ACS NANO

www.acsnano.org

ARTICLE

Flexible Electrode Arrays Based on a Wide Bandgap Semiconductors for Chronic Implantable Multiplexed Sensing and Heart Pacemakers

Thanh An Truong, Xinghao Huang, Matthew Barton, Aditya Ashok, Amr Al Abed, Reem Almasri, Mohit N. Shivdasanic, Ronak Reshamwala, Joshua Ingles, Mai Thanh Thai, Chi Cong Nguyen, Sinuo Zhao, Xiuwen Zhang, Zi Gu, Arya Vasanth, Shuhua Peng, Tuan-Khoa Nguyen, Nho Do, Nam-Trung Nguyen, Hangbo Zhao, and Hoang-Phuong Phan*

Cite This: *ACS Nano* 2025, 19, 1642−1659

Read Online

ACCESS | Metrics & More | Article Recommendations | Supporting Information

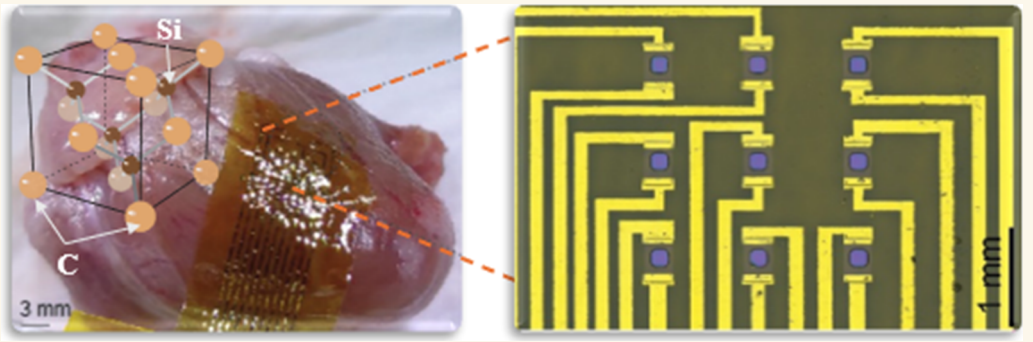

ABSTRACT: **Implantable systems with chronic stability, high sensing performance, and extensive spatial-temporal resolution are a growing focus for monitoring and treating several diseases such as epilepsy, Parkinson's disease, chronic pain, and cardiac arrhythmias. These systems demand exceptional bendability, scalable size, durable electrode materials, and well-encapsulated metal interconnects. However, existing chronic implantable bioelectronic systems largely rely on materials prone to corrosion in biofluids, such as silicon nanomembranes or metals. This study introduces a multielectrode array featuring a wide bandgap (WBG) material as electrodes, demonstrating its suitability for chronic implantable applications. Our devices exhibit excellent flexibility and longevity, taking advantage of the low bending stiffness and chemical inertness in WBG nanomembranes and multimodalities for physical health monitoring, including temperature, strain, and impedance sensing. Our top-down manufacturing process enables the formation of distributed electrode arrays that can be seamlessly integrated onto the curvilinear surfaces of skins. As proof of concept for chronic cardiac pacing applications, we demonstrate the effective pacing functionality of our devices on rabbit hearts through a set of ex vivo experiments. The engineering approach proposed in this study overcomes the drawbacks of prior WBG material fabrication techniques, resulting in an implantable system with high bendability, effective pacing, and high-performance sensing.**

KEYWORDS: *wide bandgap materials, chronic implantable devices, flexible bioelectronic interfaces, flexible heart pacemakers, long-lived heart pacemakers*

INTRODUCTION

Implantable electrode arrays for electrophysiological sensing and stimulation have an increasingly important role in monitoring, diagnosing, and treating of various health problems such as neurological[1−4] and cardiac diseases.[5−11] These systems require a large, ultrathin substrate interface with

Received: October 28, 2024
Revised: December 21, 2024
Accepted: December 27, 2024
Published: January 3, 2025

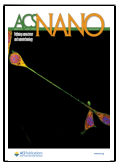

https://doi.org/10.1021/acsnano.4c15294
ACS Nano 2025, 19, 1642−1659

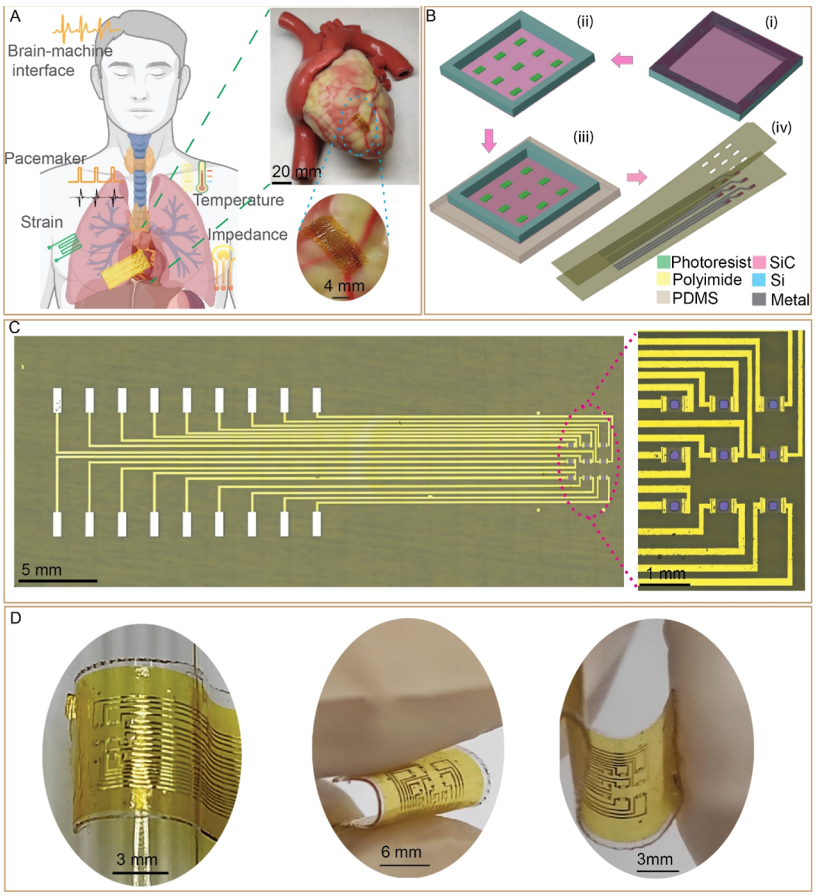

Figure 1. Device overview. (A) Schematic illustration of chronic flexible MEA for multisensing and heart pacemaker with inset highlights the free-standing flexible MEA and flexible MEA on a phantom heart model (a human model is created in BioRender. Truong, T. (2024) https://BioRender.com/n83e797). (B) Main steps for fabrication of flexible chronic MEA starting with (i) the fabrication of free-standing membranes, to (ii) the backside photolithography, to (iii) the transferring the membranes to a soft PDMS substrate for reactive ion etching (RIE), to (iv) soft transfer printing and achieving MEA with three layers: the bottom PI substrate, the functional layer of metal interconnect and SiC electrodes, the top encapsulation PI. (C) 3 × 3 MEA with 160 μm × 160 μm open windows for multiplex sensing and stimulating purpose. (D) Free-standing MEA bent around a tube with a 3 mm radius (left) and curved free-standing MEA (middle and right).

high-density electrodes to meet clinical demands for recording, sensing, and stimulating three-dimensional (3D) areas of internal tissues such as the brain, heart, and muscle surfaces.[12] In addition to high spatial resolution, the flexibility of implantable electronic devices is a critical criterion to allow conformal interfacing with soft, curvilinear, and dynamic tissues. Therefore, the encapsulation of functional layers becomes a crucial element to isolate metal interconnects, integrated bioamplifiers, and multiplexed components (e.g., in the form of nanomembrane transistors) from biofluids, extending the lifespan of implantable devices.[13] Acting as electrical barriers between electrodes and tissues, encapsulating layers with precise openings for recording and stimulation electrodes mitigate crosstalk and strategically reposition functional layers closer to the neutral mechanical plane (NMP) of the multilayered structure. This strategic placement reduces stress concentrations, a crucial consideration given the high bendability required for interaction with 3D organs and tissues.

Representative examples of the clinical applications of implanted electrodes include heart pacemakers and cardioverter-defibrillators (ICD), which play a critical role in effective cardiac rhythm management. While conventional heart pacemakers and ICD have demonstrated their effectiveness in the treatment of cardiovascular diseases such as arrhythmias[14,15] and heart failure,[16,17] their mechanical rigidness poses several limitations including the high invasiveness, tissue damage due to their mechanical mismatch with 3D soft tissue surfaces and complex motions of cardiac tissues, clot formation, and malfunction of devices.[18,19] Flexible heart pacemakers address these limitations of their rigid counterparts, providing a promising solution for long-term cardiac rhythm management. Their flexibility enables a conformal interface with cardiac tissues' dynamic and three-dimensional nature, enhancing device performance. Functional polymers have been investigated widely for implantable health monitoring.[20−25] The use of multielectrode array (MEA) configurations enables multisite stimulation on the heart surface rather than inducing a high electrical potential to a predefined position in the conventional bipolar electrode pacemakers.[10] For long-lived heart pacemakers and ICD, the device stability becomes crucial to ensure prolonged functionality and adaptability within the ever-changing physiological environment of the human heart. As such, the use of gold (Au), an inert metal, as the interfacing electrode with cardiac tissues has been explored.[26−28] Nevertheless, previous studies reported the possibility of biofluids diffusing through the polycrystalline metal electrodes, which potentially leads to lethal events associated with leakage

https://doi.org/10.1021/acsnano.4c15294
ACS Nano 2025, 19, 1642−1659

currents.[29] The narrow potential window in noble metal or carbon fibers is another source of potential failure due to water electrolysis and gas bubble formation at high stimulation voltages.[30]

In recent years, wide bandgap (WBG) materials, exemplified by silicon carbide (SiC), gallium nitride (GaN), and diamond, have been employed widely in harsh environments due to their excellent inertness and mechanical and electrical stability. These materials also offer excellent transparency, enabling optical mapping and observation of the internal tissues. Bulk materials of WBG semiconductors are used in implanted glucose sensors, neural electrodes, and physical sensing,[31] but their rigidness can potentially cause tissue injuries. Therefore, soft, implantable thin films grown on a soft substrate and physically transferred onto soft polymers represent an attractive approach to creating flexible bioelectronic interfaces. Representative examples of WBG systems for long-term, flexible bioimplants include SiC thin films. Amorphous SiC (a-SiC), which can be deposited at low temperatures, has been employed as an encapsulation layer for chronic neural recording and stimulation[32,33] due to its robustness and low dissolution rate compared to conventional bio barrier layers such as silicon dioxide (SiO_2).[34] However, amorphous materials typically contain a high density of defects and pinholes,[35] which are detrimental to biobarrier performance. The presence of pinholes and defects necessitates a relatively large film thickness to prevent water and ion diffusion, thereby compromising the mechanical flexibility of a-SiC. Additionally, amorphous materials exhibit low electrical conductivity and high impedance, making them suboptimal for recording and stimulation. Coating metal on top of a-SiC as presented in previous study raises concerns about the longevity of the electrode.[33] Nanocrystalline SiC has been utilized as alternative for long-term recording electrodes;[32] however, the defect-rich boundaries between crystalline grains impedes charge carrier mobility, resulting in lower electrical performance compared to crystalline materials. In contrast to a-SiC, pinhole-free, highly conductive crystalline SiC nanothin films emerge as a promising candidate for long-term stable biointerface (A detailed comparison between different polytypes of SiC is presented in Table S1). Recent studies have integrated crystalline SiC electrodes into flexible substrates such as polyimide (PI)[36,37] and polydimethylsiloxane (PDMS).[38] Nevertheless, these studies have not considered relocating the metal interconnect and electrode layers to the NMP, resizing the devices, and constructing MEA configurations, which are imperative for multiplexed sensing, recording, and stimulating.

This paper utilizes double-sided photolithography on free-standing SiC membranes and transfer printing techniques to develop MEAs in WBG material for multiplexed sensing and stimulating. This method encapsulates metal interconnects, strategically relocates SiC to the NMP to allow for small bending curvatures, and scales up the number and size of electrodes. The fabricated devices demonstrate exceptional bendability coupled with proficient physical sensing, stimulation, and recording capabilities. The application of the MEA as a heart pacemaker is demonstrated using a rabbit's heart model. Additionally, the long-term biocompatibility of the MEAs was validated through in vivo experiments. Strategies for decoupling multisignal noise and enhancing the electrochemical performance of the electrodes are also proposed and discussed. The design concept and results in this paper establish a novel pathway for engineering and utilization of WBG nano thin films in chronic implantable devices.

RESULTS AND DISCUSSION

Design Features. Figure 1A illustrates the versatility of SiC flexible devices for chronic implantation, including physical sensing (e.g., strain and temperature), electrophysiological recording (e.g., neural signals), and stimulation (e.g., heart pacing). The implantable device comprises SiC electrodes connected to metal interconnects sandwiched between two flexible PI substrates (Figure 1B). For applications that require direct contact between SiC electrodes and tissues, openings in the encapsulation are created to expose the electrodes. The longevity of SiC electrodes was confirmed through a hydrolysis test, revealing their stable electrical conductivity over months in phosphate buffered saline (PBS) 1× solutions at 80 °C (Figure S1). Furthermore, we demonstrated that Pt and Au electrodes are eroded quickly in PBS 1× solution, as shown in Figure S2. The chemical stability of the SiC membrane over commonly used gold (Au) and platinum (Pt) of uniform thickness (200 nm) is characterized through an accelerated etching test in 1× PBS. A series of voltametric tests were performed under an extended potential window of ±2 V for all the materials. Under such conditions, the higher applied potential facilitates a faster redox reaction, causing the surface atoms to react faster with the PBS electrolyte. Through this process, we observe that the SiC membrane (Figure S2A) remains robust even after 10 redox cycles. It was evident that within 2 and 7 redox cycles, Au undergoes a complete etching and Pt is partly etched away, respectively, shown in Figure S2B,C. Therefore, the SiC material is more suitable for long-lived implantable electrodes. The utilization of nanoscale functional layers (SiC and metal traces) and an intrinsically soft substrate (PI) facilitates excellent conformal contact with internal organs and tissues, as shown in Figure 1A (inset). The optical transparency of SiC represents attractive features for concurrent electrical recording and optical mapping.[39] This transparent MEA also allows real-time observation without optical interference and light delivery to the accurate area of internal tissues with microscale resolution.

We combined our double-sided photolithography technique[37] with the transfer printing method to create SiC patterns onto a polymer thin film, where SiC free-standing membranes serve as the template. The transfer process started by depositing a 100 nm-thick metal layer (aluminum) onto the front side of the membranes, followed by a photolithography process and wet etching to define the metal patterns (Figure S3 (up)). Employing a back-side photolithography process, we aligned photoresist microstructures with the metal patterns on the front side of the membranes. These metal patterns served as a protective layer to mitigate the risk of fracture during stamping steps, which is crucial for preserving fragile SiC layers. Before laminating the front side of the SiC membranes onto a PDMS (ratio 10:1) sheet, a thin layer of positive photoresist (ECL 3012) was spin-coated on the front side to cover the entire SiC surface. This photoresist layer played a crucial role in reducing adhesion between the micro patterns and the PDMS, thereby enhancing the stamping yield. The membranes on PDMS samples (Figure S3 (down)) were then laminated onto a glass slide before selectively etching away unwanted SiC using RIE. Next, a sacrificial 100 nm poly(methyl methacrylate) (PMMA) layer was spin-coated

https://doi.org/10.1021/acsnano.4c15294
ACS Nano 2025, 19, 1642−1659

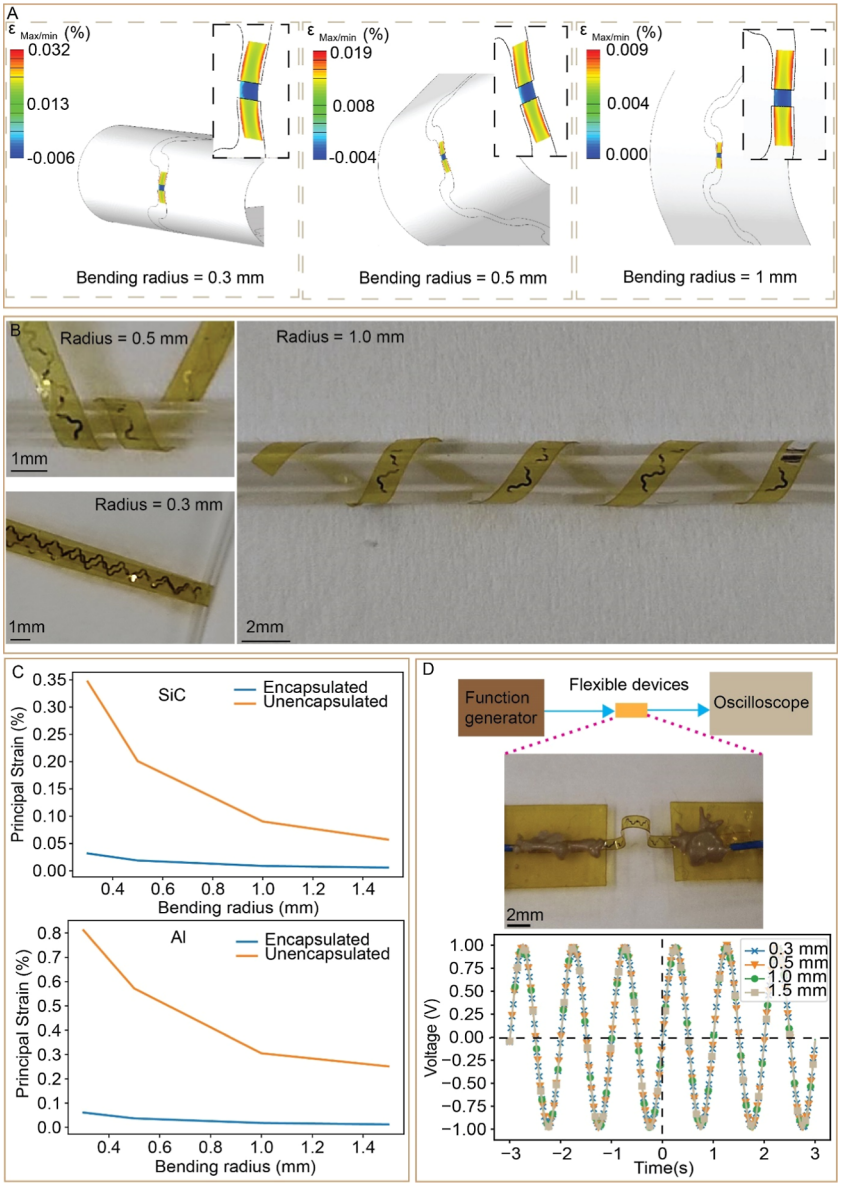

Figure 2. Mechanical flexibility of the mesostructure. (A) FEA simulation of an encapsulated strain sensor bending around different bending radii. The insets show the zoomed-in FEA image of the SiC layer. The contours in the FEA images display the maximum and minimum principal strains in the SiC layer. (B) Optical images of a flexible encapsulated electrode bending around the circular tube with different radii. (C) Maximum principal strains on SiC (top) and maximum equivalent strains on Al (bottom) for the devices with and without the encapsulation layer. (D) Output characteristics of an encapsulated electrode in response to an ac input of 1 V at 1 Hz after bending with different bending radii.

on the glass slide, followed by spin-coating a layer of PI on top of the PMMA layer. After soft baking the PI at 110 °C for 35 s, the SiC pattern of the PDMS sheet was stamped onto the PI layer. Subsequent removal of the photoresist layers using acetone and isopropanol and curing the PI at 200 °C for 1 h was followed by depositing metal on top of the glass slide sample. A photolithography and wet etch process defined the interconnection patterns, and a layer of PI was spin-coated on top of the sample. Open windows were created at the desired positions to expose the SiC electrodes for the impedance sensor and stimulation electrodes. Finally, the encapsulation PI layer was cured at 260 °C for 1 h, ensuring the mechanical and chemical properties of fully cured PI film. Detailed information on the fabrication process is presented in Supporting Information Note S1 and Figure S4.

The surface areas of implantable devices are critical as they must adhere to the need for minimal invasiveness within the human body, while certain applications demand larger and elongated devices, such as in deep brain stimulation, neural nerve stimulation, and heart pacemakers. We have successfully expanded the size of the flexible device up to 50 mm for strain sensors (Figures 1C and S5), surpassing the limits (5 mm × 5 mm) set by previous studies.[36−38,40] The device size is solely constrained by the dimensions achievable through the standard photolithography process. This scalability is also evident in the number of electrodes, accommodating configurations from a single electrode to various MEA, such as 3 × 1, 3 × 3, and potentially 4 × 5 (Figure S6) electrode arrays. The technique of double-sided photolithography on free-standing membranes has been demonstrated to be effective for various WBG

https://doi.org/10.1021/acsnano.4c15294
ACS Nano 2025, 19, 1642−1659

materials, ranging from SiC to wider bandgap materials such as GaN and SiN.[37] Simultaneously, the transfer printing technique enhances the versatility of our approach, making it suitable for the fabrication of MEA by using several WBG materials. To improve system stretchability, we employed serpentine-shaped structures for the metal traces and the PI substrate[41] (Supporting Information Note S2 and Figure S7). The fabrication method for these structures is also shown in Figure S8.

Figure S5 presents an integrated multiplexed sensing and stimulation system comprising a temperature sensor, a strain sensor, and an array of SiC electrodes for impedance sensing and electrical stimulation. The utilization of a stamping technique enables the production of multiple electrodes exhibiting diverse orientations (e.g., ⟨100⟩ and ⟨110⟩), shapes (e.g., circles and rectangles), and sizes, which can be customized for various sensing and stimulating objectives. For instance, n-type SiC with ⟨100⟩ crystallographic orientation was selected for temperature sensing as it is less sensitive to mechanical impact. On the other hand, we employed n-type SiC aligned along the longitudinal ⟨110⟩ direction for strain monitoring due to the high piezoresistive coefficient in this orientation. The dimensions of both electrodes and open windows are highly adaptable, permitting an increased charge injection capacity for stimulating purposes or reduced sizes to enhance stimulation and sensing resolution. Figure 1D presents the flexibility of the as-fabricated electrode arrays that can be wrapped around or bent into cylindrical shapes with a bending radius as small as 1.5 mm bending radius.

Mechanical Flexibility of Devices. The flexibility of the mesostructure is crucial in implantable devices, as it enables optimal conformity to the 3D contours of bodily tissues. To assess the mechanical adaptability of our current devices, we utilized theoretical calculations to determine bending stiffness and conducted finite element analysis (FEA).

The bending stiffness (EI) of the multiple layers is calculated as[42]

$$EI = \sum_{i=1}^{N} E_i h_i w \left[(y_0 - \sum_{j=1}^{i} h_j)^2 + (y_0 - \sum_{j=1}^{i} h_j) h_j + \frac{1}{3} h_i^2 \right] \quad (1)$$

where $N = 4$ is the number of layers (i.e., layer 1: PI, layer 2: SiC, layer 3: Al, layer 4: PI) and y_0 is the position of the NMP

$$y_0 = \sum_{i=1}^{N} E_i h_i \left[\left(\sum_{j=1}^{i} h_j - \frac{1}{2} h_j \right) \left(\sum_{i=1}^{N} E_i h_i \right)^{-1} \right] \quad (2)$$

where E_i, h_i, and w are the elastic modulus, thickness, and width of each layer, respectively. We assume that the width of the Al layer is the same as that of the PI substrate (1 mm), which is the worst scenario since Al possesses a higher elastic modulus than the PI material. The SiC electrode is small (70 μm × 200 μm) and thin (200 nm); therefore, its contribution to the stiffness of the thin film is negligible. Accordingly, the bending stiffness of the entire structure was found to be 14.110^{-12} N·m^2, which ensures optimal contact of the electrode with the three-dimensional and intricate shapes of human organs and tissues.[43] Equation 1 also reveals that the flexibility of the mesostructure is proportional to the cube of each layer' s thickness, making it crucial to maintain the thickness at the nanoscale to ensure mechanical match with the soft biology tissues. We further conducted FEA to assess the flexibility of the devices. Increasing the thickness of functional layers to 1 μm may lead to fracture at the interface of metal and SiC electrode as shown in Figure S9. Figure 2A illustrates the strain distribution in the SiC electrode with dimensions of 70 μm × 200 μm in a fully encapsulated structure, and Supporting Information Figure S10 also shows the strain distribution of the Al layer with a size of 90 μm × 16 mm in the same structure. The cross-sectional view of the structure is depicted in Supporting Information Figure S11. The FEA results of a free-standing flexible structure, extracted from the multiplexed array via laser cutting (Figure S5), reveal that the strain levels are well below the respective tensile fracture strain of thin-film SiC (i.e., 0.28%)[44,45] and thin-film Al (10%).[46]

The FEA compares the strains between encapsulated and unencapsulated structures when bending around tubes of radius from 0.3 to 1.5 mm considering the smallest bending radius to align with the reported diameter of neural nerves in infants.[47−51] Figures 2C and S8 show the strain distribution on functional layers at a bending radius ranging from 0.3 to 1.5 mm. Notably, unencapsulated SiC layers at a bending radius of 0.3 mm exceed their fracture strain (0.28%) (Supporting Information Figure S12), potentially leading to device failure. In contrast, the maximum strain in encapsulated SiC layers remains at 0.03% (Figure S10), significantly lower than the fracture strain of SiC. Similarly, while unencapsulated Al layers pose significant fracture risks, the maximum strain in the encapsulated layer is well below the tensile strain of the Al thin film. This smaller strain is attributable to the encapsulation layer, relocating the semiconductor and metal layers closer to the mechanical neutral axis of the entire structure.

The encapsulation of functional layers can effectively mitigate the impact of substrate thickness on the stress levels within these layers. We performed the FEA with a bending radius of 0.3 mm to examine the stress level in the functional layers as the substrate thickness varies. Without encapsulation, a slight increase in substrate thickness from 3 to 4 μm resulted in a significant increase in strain for both SiC (from 0.24% to 0.347%) and Al (from 0.440% to 0.811%). Conversely, the presence of an encapsulation layer maintained low and stable strain levels, keeping them below the fracture strain of each material, even when the substrate thickness was increased to 10 and 15 μm.

Figure 2B shows optical images of the fabricated devices, bent around tubes with radii of 0.3, 0.5, and 1 mm. These bending structures underwent testing to examine the occurrence of fractures by connecting one connector pad to a function generator and the other to an oscilloscope. A sinusoidal input signal of 1 V magnitude and 1 Hz frequency was generated by the function generator transferring through the flexible device to the oscilloscope. The results revealed identical signals across different bending curvatures, indicating that no fractures occurred in the devices (Figure 2D).

It is worth noting that encapsulating the functional layers mitigates the effect of substrate thickness on the strain in these layers, as shown in Figure S13. For example, without encapsulation, the strain in the Al layer nearly doubles from 0.44% to 0.811% as the substrate thickness increases from 3 to 4 μm. However, with encapsulation, the strain in both SiC and Al layers experiences little change and remains much smaller than that of their fracture strains.

https://doi.org/10.1021/acsnano.4c15294
ACS Nano 2025, 19, 1642−1659

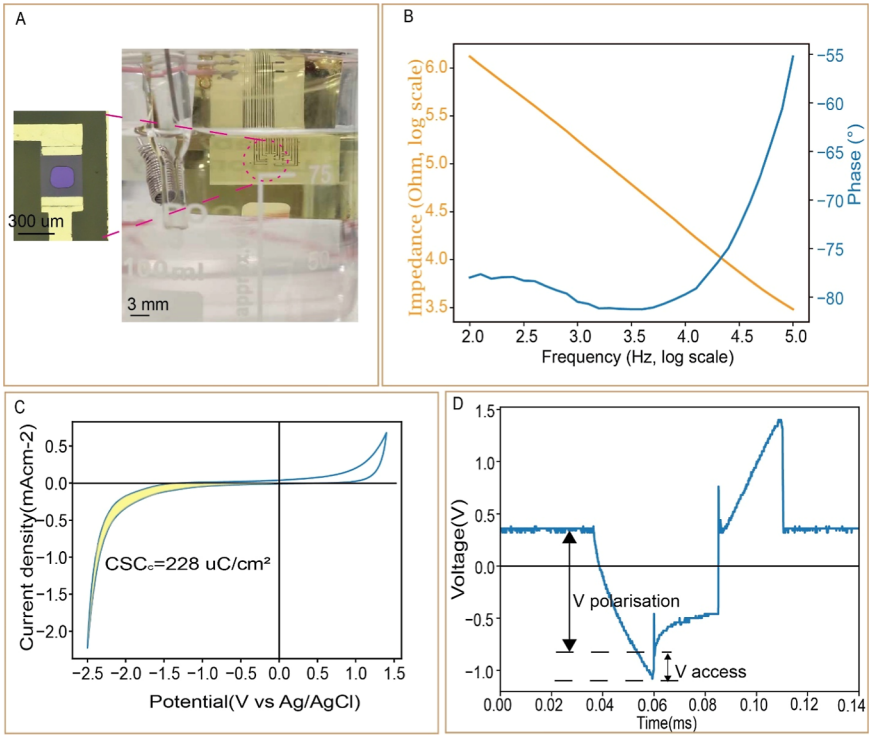

Figure 3. Electrochemical characterization of a SiC implantable electrode. (A) Optical image of an MEA laminated on a glass slide in a PBS 1× solution with platinum (Pt) counter electrode and Ag/AgCl reference electrode. (B) Electrochemical impedance and phase-angle spectra of the SiC electrode in PBS 1× solution. (C) Cyclic voltammograms of a SiC electrode at scan rate of 0.5 V/s. (D) Voltage transient response of a SiC electrode with respect to a biphasic symmetric cathodal first current of amplitude 100 μA, 25 μs per phase, and 25 μs interphase gap.

Further, FEA was conducted for a single electrode in a 3 × 3 MEA since the open window on top of the SiC electrode moves the SiC in the window area further away from the NMP of the multilayered structure. Supporting Information Figure S14 shows two bending directions where the window is facing inward and outward of the bending direction. When the open window is facing outward, the SiC electrode is under tension, and the results indicate that the maximum tensile strain occurs along the edges of the open window parallel to the longitudinal axis of the structure. At a 0.3 mm bending radius, this maximum strain reaches 0.46%, surpassing the fracture strain of SiC.[44,45] However, other areas of the SiC window and Al exhibit strains below their fracture strain threshold, suggesting no fractures in those regions. Increasing the bending radius to 0.5 mm decreases the maximum strain below the fracture strain. Since most organs and nerves have convex surfaces, the SiC electrodes experience compressive strain when directly interfacing with these surfaces. The results indicate that the maximum compressive strain (0.49%) at 0.3 mm bending radius occurs in the similar region. However, studies show that SiC have larger fracture strain in compression (0.8−1.4%) than in tension.[52,53] Therefore, our SiC electrodes should remain functional without fractures on most organ surfaces.

Electrochemical Characterization of Stimulation Electrodes. The design of the SiC MEA serves as a new platform for the stimulation and recording of electrochemical signals. Evaluation of the recording and stimulating capabilities of the SiC MEA involves electrochemical impedance spectroscopy and cyclic voltammetry (CV) measurements using the setup in Figure 3A, where Pt is employed as the counter electrode and Ag/AgCl serves as the reference electrode. Figure 3B presents the impedance and phase of a SiC electrode in a 1× PBS 1× solution. At a frequency of 1 kHz, the impedance is approximately 180 kΩ, and the phase is 80°, indicative of a capacitive electrode/electrolyte interface. The charge storage capacity (CSC), a crucial parameter for quantifying stimulation performance, is assessed through CV scans over a 25,600 μm^2 geometric surface area (GSA) of the SiC electrode. The results demonstrate no distortion of the CV shape even at a high scan rate of 0.5 V/s, underscoring the excellent electrochemical stability of the electrode.

CV scan was performed from −2.5 to 1.4 V as shown in Figure 3C. There is a significant hydrogen evolution (HER) at −2.5 V and oxygen evolution reactions (OER) at 1.4 V. In several studies, the potentials where these reactions begin to occur are used to define the usable water window.[54,55] In our electrodes, the onset of water reduction, where HER starts to occur, is approximately −1.4 V, and the onset of water oxidation, where the OER begins, is around 1 V. This results in a usable water window of about 2.4 V for our material. It is also important to note that Pt exhibits strong water reduction at −0.6 V; despite this, the water window for Pt is typically stated between −0.6 and 0.8 V.[56]

The CSC is calculated as

$$\mathrm{CSC} = \int_{E_c}^{E_a} \frac{|i| dE}{\nu A} \tag{3}$$

where i, E, ν, and A are the measured current, applied voltage, scanning rate, and active area of the SiC electrodes, respectively. Based on eq 3, the CSC of the SiC electrode was found to be 417 $\mu C/cm^2$, with a cathodic CSC (CSC_c) of 228 $\mu C/cm^2$. We performed CV scans at different rates,

https://doi.org/10.1021/acsnano.4c15294
ACS Nano 2025, 19, 1642−1659

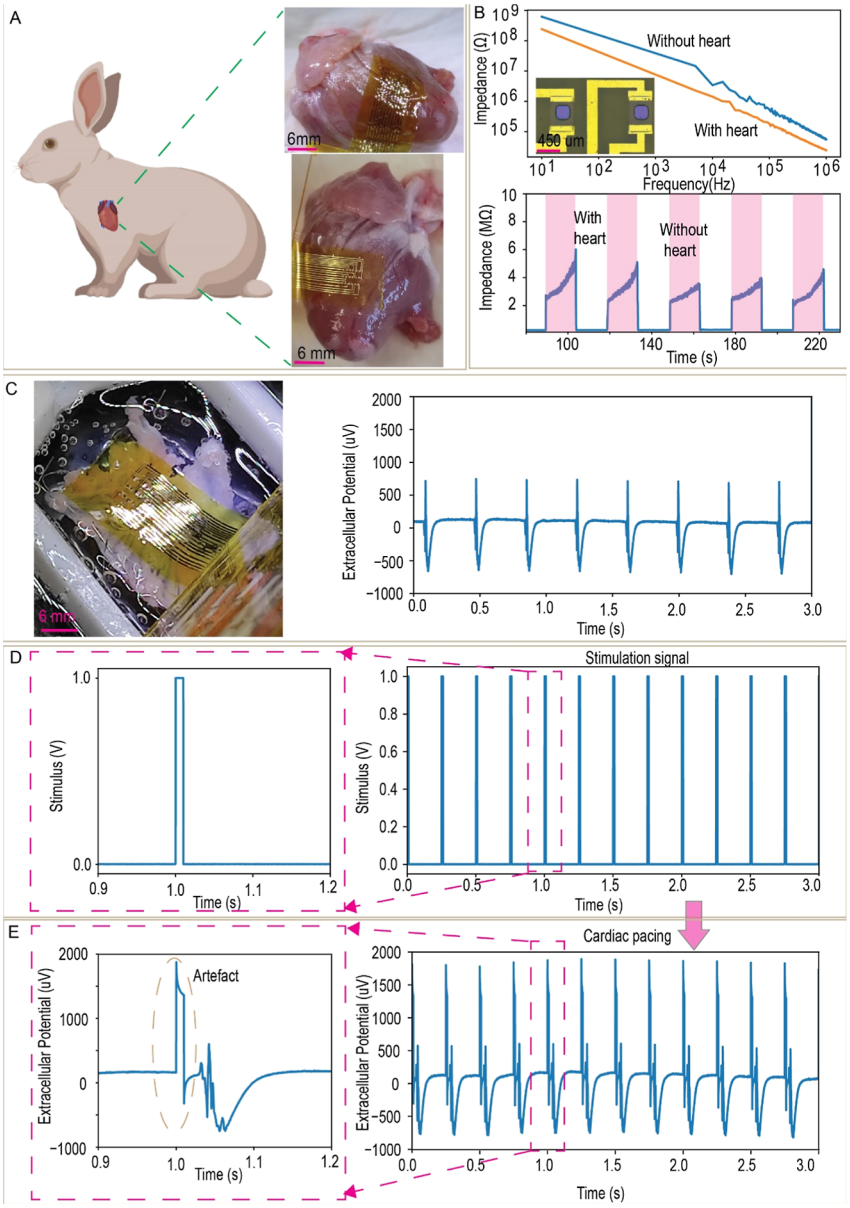

Figure 4. Ex vivo study of a flexible SiC heart pacemaker. (A) (Left) Illustration of a flexible SiC heart pacemaker of 3 × 3 MEA in good contact with rabbit's heart (right); the rabbit model is created in BioRender. Truong, T. (2024) https://BioRender.com/w94e687. (B) Impedance sensing of a pair of electrodes from 3 × 3 MEA with and without heart tissue. (C) (Left) Optical image of a flexible MEA heart pacemaker on top of a heart tissue lying inside the medium (right). Extracellular potential of the heart tissues without stimulation. (D) Stimulation signal. (E) Extracellular potential of the heart tissues with a 4 Hz stimulation.

ranging from 50 to 500 mV/s from the symmetric potential of −1.4 to 1.4 V, to determine the double-layer capacitance of the electrode (Figure S15A). Linear fitting of current versus scan rate at a potential of 0 V revealed a double-layer capacitance of 15.54 nF (Figure S15B), indicating the potential for recording capability.

The charge injection limit (Q_{inj}) is another pivotal parameter for quantifying the stimulation capability of an electrode. To determine Q_{inj}, electrodes were subjected to a constant current biphasic cathodic-first charge-balanced pulse against a 25,600 μm^2 GSA. Considering an onset water reduction of −1.4 V, a constant current biphasic cathodic-first charge-balanced pulse against the working SiC electrode with an amplitude of 100 μA, phase width of 25 μs, and interphase of 25 μs resulted in maximum polarization with a charge injection limit of 9.8 $\mu C/cm^2$ for the SiC electrode (Figure 3D). This charge injection limit exceeds the threshold required for several vision and hearing stimulating applications such as stimulating of epi-retinal, optic nerve, and auditory brainstem.[56] Considering a cathodic polarization voltage (V polarization) equal to the cathodic water window of the electrode (−2.5 V) as shown in Figure S16, a pulse with an amplitude of 150 μA, phase width of 50 μs, and interphase of 50 μs was applied, which resulted in the V polarization equal to 2.5 V. A Q_{inj} of 29 $\mu C/cm^2$ was calculated from the applied pulse, surpassing the threshold requirements for various neural prostheses such as the auditory brainstem, subthalamic nucleus in humans, and for sciatic nerve or interfascicular in cats.[56]

Ex Vivo Study of a SiC Heart Pacemaker. To investigate the biocompatibility of the materials, an in vitro cell viability

https://doi.org/10.1021/acsnano.4c15294
ACS Nano 2025, 19, 1642−1659

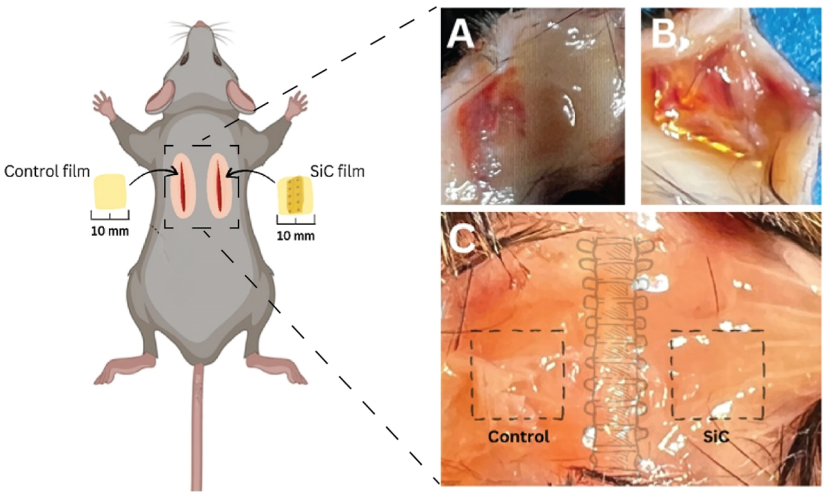

Figure 5. Optical images of tissue in contact with the implanted films. (Right) Schematic illustration of surgical process. (Left) (A) subcutaneous pocket with a control film, (B) subcutaneous pocket with a SiC film, and (C) connective tissue muscle interface where films were placed (see broken line box).

assay was conducted using fibroblast cell NIH/3T3 as a well-accepted population for investigating biocompatibility. We hereby incubated NIH/3T3 cells with the SiC membranes used in this study. As shown in Supporting Information Figure S17, the 3-(4,5-dimethylthiazol-2-yl)-2,5-diphenyl tetrazolium bromide (MTT) assay showed an increased absorbance value at 570 nm wavelength after 24-, 48-, and 96 h incubation, indicating cell growth and desirable viability of cells cultured on the SiC membrane. Microscopic images taken at different time intervals further revealed the increasing cell densities in response to the SiC membranes, which further demonstrated the biocompatibility of the SiC membranes.

We demonstrated the pacing functionality of our flexible device by using ex vivo experiments. The sinoatrial node and surrounding right atrial pectinate muscle tissues were obtained from the heart of a New Zealand White rabbit (tissue sharing arrangement, UNSW Animal Care and Ethics Committee approval protocol 22/101A), which was maintained with Krebs-Ringer solution and mounted in a recording chamber. The mechanical flexibility of SiC on PI along with the engineering design that brings functional components close to the neutral axis enable conformal contact between the device and the curvilinear surface of the heart as shown in Figure 4A. The optical transparency of the SiC electrode is another compelling feature that could facilitate observation through the stimulated area and enable optoelectronic study, Figure S18. While chemical inertness is a key property for long-term implants, optical transparency offers additional functionalities that can enhance the physiological recording and analysis. Optical transparency in SiC is achieved thanks to its large optical bandgap, which minimizes photoenergy absorption at visible wavelengths. This is not the case for a standard silicon material. Recent studies have suggested the advantages of transparent electrodes that allow for simultaneous electrophysiological recording and optical mapping (e.g., calcium imaging). Electrophysiological recording offers a fast response on the order of milliseconds to microseconds, while optical mapping provides spatial resolution of cellular activities. A combination of the two measurement methods helps to overcome the technological limitations of each individual technique.

Integration of multiple electrode arrays allows for simultaneous physical contact measurement and electrical stimulation. Specifically, as illustrated in Figure S19, we employed a pair of electrodes (1 and 4) as working electrodes and another pair (6 and 9) as return electrodes, strategically chosen to maximize the geometrical surface area. Concurrently, electrodes 2 and 5 function as impedance sensors to detect contact between the electrodes and heart tissues. Figure 4B (top) plots the measured impedance with and without contact with cardiac tissue, while Figure 4B (bottom) exhibits the repeatability of impedance sensing at 1 kHz.

Figure 4C shows the experiment setup (left) and the action potential of the rabbit heart tissue before stimulation. Figure 4D shows the stimulus signal waveform with an amplitude of 1 V, which is well within the water window of SiC electrodes. The monophasic electrograms are shown in Figure 4E, demonstrating the successful pacing and activation of rabbit cardiac neurons with a phase-locked response. Supporting Information Figure S20 displays the action potential recordings before and during electrical stimulation using the SiC electrodes across all stimulus intensities from 1.3 to 7 V. These results highlight the capacity of our flexible device to pace heart tissues effectively, even at potentials significantly exceeding its water window. Cardiac pacing, induced by the electrical stimulation of the electrodes, results in a notable alteration of the tissue's intrinsic pacing rate from 2.6 Hz (Figure 4C) to 4 Hz (Figure 4E), aligning with the applied stimulation frequency. This substantial modulation underscores the profound impact of the SiC electrodes on the pacing dynamics of cardiac tissue, offering a foundation for potential translation into chronic in vivo testing and ultimately clinical trials.

Spontaneous pacing was also recorded via the SiC electrode, which yielded stable monopolar electrograms. Although the noise floor in the measurements ($V_{S.D}$ = 7.8 μV) is slightly higher compared to gold standard recordings ($V_{S.D}$ = 1.9 μV) using the tungsten electrode, the cardiac waveforms demonstrate the ability of SiC electrodes to resemble the fine signal features observed in the conventional bioamplifier measurements (Figure S21). We calculated the SNR as $\mathrm{SNR\,(dB)} = 10\log_{10}\frac{\mathrm{Signal}}{\mathrm{Noise}}$. The SNR from the recording data

https://doi.org/10.1021/acsnano.4c15294
ACS Nano 2025, 19, 1642−1659

is −0.25 dB, indicating that the noise power is slightly greater than the signal power. While we can see that the noise level in the recordings appears relatively high, the demonstration of signal acquisition post filtering from such small and delicate preparations highlights the compatibility of SiC electrodes with electrophysiological applications.

In Vivo Study for Long-Term Biocompatibility of SiC MEAs. Studying the biocompatibility of SiC MEAs is essential for ensuring their suitability in long-term applications. In this study, we conducted in vivo experiments on four adult mice. Control films and 10 mm × 10 mm SiC MEA films were implanted in the left and right dorsal pockets, respectively (Figure 5). After 1 week of implantation, a macroscopic evaluation was performed using optical imaging of the film-tissue interface and a semiquantitative morphological analysis to assess acute inflammation, purulent exudate, localized necrosis, and implant rejection. Additionally, inflammatory responses and morphological changes surrounding the implanted films were examined by using light microscopy. More details can be found in the Method section.

Macroscopic Evaluation. Animals were monitored twice daily for the first 48 h postimplantation and thereafter once daily to assess for any signs of implantation-related abnormalities or welfare concerns. All animals survived the duration of the study, and no behavioral changes or indications of infection were observed at any time. The implantation of both film types did not result in any surgery-related or implantation-related complications. However, one animal reopened the surgical site at the control film implantation area less than 24 h before the conclusion of the study.

Throughout the study period, no visible signs of inflammation, discharge, or ulceration were observed in the skin over the implanted films. Upon euthanasia, mild subcutaneous inflammation was noted adjacent to the implantation sites of both the control and SiC films (Figure 5A,B, respectively). No signs of inflammation, fibrosis, necrosis, or purulent exudate were observed at the muscle-connective tissue interface, where the films were placed (Figure 5C).

Microscopic Evaluation. The histopathological evaluation assessed host tissue responses following the subcutaneous control and SiC films' implantation over 7 days. Histological analysis was performed on skin sections in direct contact with the control films (Figure 6A,B) and SiC films (Figure 6C,D), as well as the tissue (connective tissue and skeletal muscle) immediately underlying the implanted control and SiC films (Figure 6E,F, respectively). Hematoxylin and eosin (H&E) staining was used to evaluate various biocompatibility parameters, including tissue pocket thickness and cellular infiltration. The H&E-stained skin samples revealed typical histological architecture in all specimens, regardless of the group (control vs SiC). There was no evidence of excessive inflammatory infiltrates, exudates, fibrosis, or adverse tissue reactions in either the skin or the underlying connective-muscle tissue. Tissue thickness in contact with the implanted films showed no significant difference between the control and SiC groups. Additionally, there was no evidence of neovascularization surrounding the films, which further supports the biocompatibility.

Multimodal Sensing Performances of Flexible SiC Platforms. Flexible implantable thermal sensors have been utilized to monitor the rejection status of transplanted kidneys[57,58] and heart function. We demonstrated the

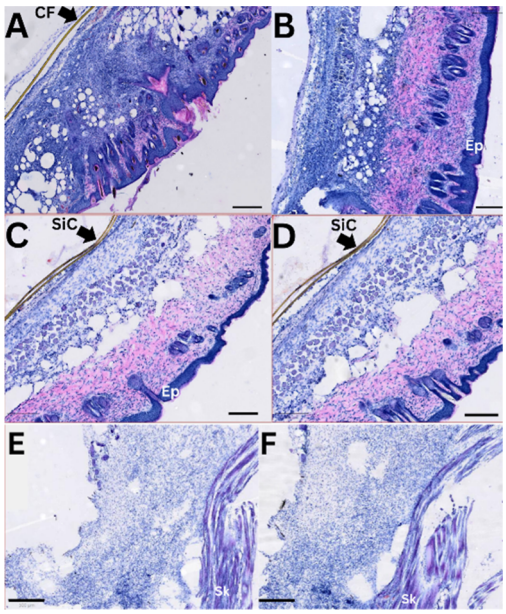

Figure 6. Hematoxylin and eosin-stained histological sections of tissue surrounding films. (A,B) Cross section of skin of control samples. (C,D) Cross section of skin of SiC film samples. (E) Connective tissue—muscle interface where control films were placed. (F) Connective tissue—muscle interface where SiC films were placed. All samples were imaged at ×10 magnification. A−D samples scale bar 200 μm, E,F scale bar 500 μm. CF control film, SiC silicon carbide, Ep epidermis, Sk skeletal muscle.

temperature sensing capability in the as-developed platform employing a 300 μm × 450 μm SiC resistance with a 160 μm × 160 μm open window, as depicted in Figure 7A (upper left corner). The sensor, laminated on a glass slide, was placed on a hot plate to assess the sensitivity. Figure 7A (right) illustrates the linear current−voltage characteristics of the electrode across a temperature range from 25 to 100 °C, confirming the Ohmic contact between the metal and the SiC electrode. The inset reveals a decrease in current corresponding to an increase in temperature, indicative of an elevation in resistance. This increase in resistance is attributed to increased lattice scattering, resulting in a decrease in electron mobility (μ). The semiconductor resistivity is calculated as

$$\rho = \frac{1}{nq\mu} \tag{4}$$

where q is the electron charge.

An increase in the temperature (T) also increases the electron concentrations (n) according to eq 5.

$$n \sim T^{\alpha} \exp\left(\frac{-E_a}{kT}\right) \tag{5}$$

where E_a is the activation energy, α is the coefficient of thermal expansion, and k is the Boltzmann constant. However, in highly doped semiconductors, the lattice scattering is more dominant than the increase in carrier concentration, causing an increase in the resistance. Supporting Information Figure S22 shows the linear fitting of the change in resistance versus the change in temperature of our SiC electrode, indicating a thermal coefficient of resistance (TCR) of 607 ppm/K.

The linear relationship between electrical resistance (R) and temperature (T) can be expressed as

https://doi.org/10.1021/acsnano.4c15294
ACS Nano 2025, 19, 1642−1659

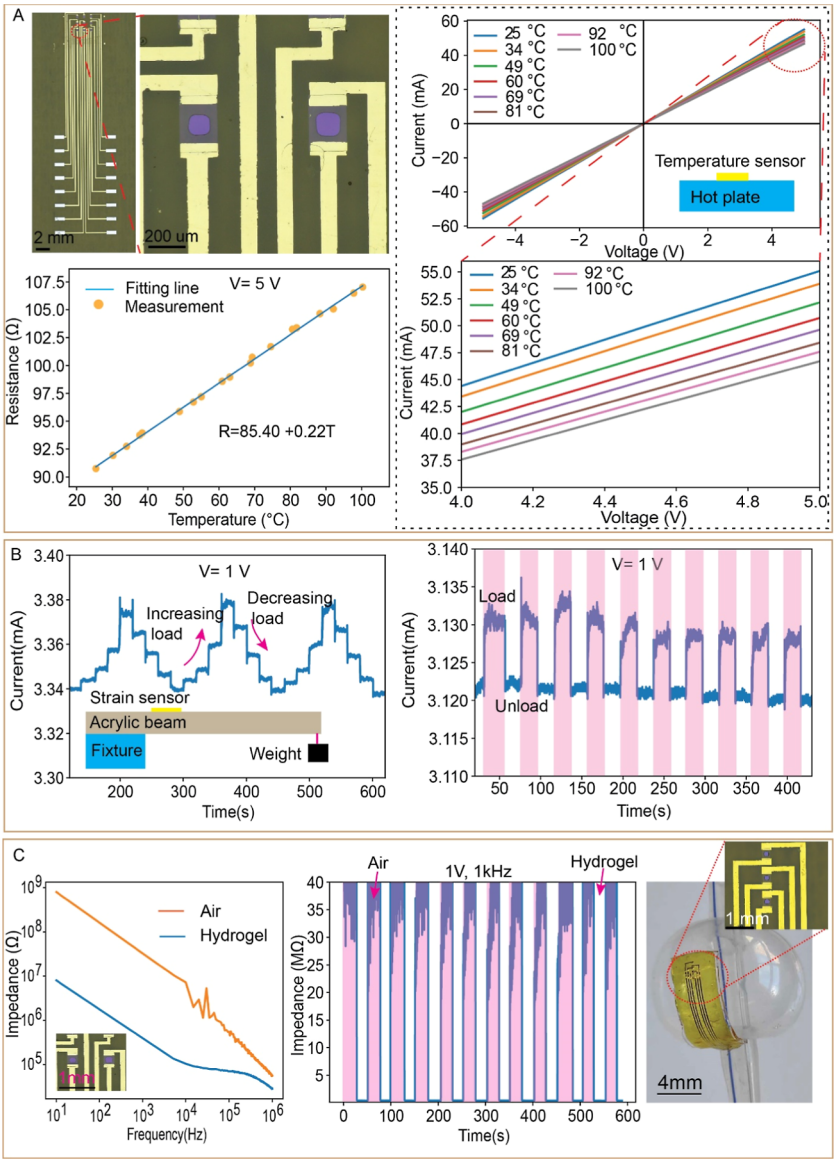

Figure 7. Physical sensing characterization. (A) Temperature sensing: (upper left corner) A 3 × 3 MEA electrode used for physical sensing characterization, (right) current−voltage (*IV*) characteristic of a sensor under different temperatures with inset in the range of 4 to 5 V (bottom left corner), bottom left: resistance change vs temperatures (root-mean-square deviation of the fitting line: 0.28). (B) Strain sensing: (left) sensitivity of a sensor under increasing and decreasing load, (right) repeatability of the electrode under cyclic load. (C) Impedance sensing: (left) the impedance measured with and without the PVA hydrogel of an impedance sensor made from a pair of electrodes, (middle) the repeatability of the impedance sensor with several cycles of touching and untouching the hydrogel, (right) a transparent array of the electrode bonded to a catheter balloon as an illustration of MEA implementation on a soft robot actuator for cancer detection and real time observation.

$$R = R_0 + \alpha(T - T_0) \tag{6}$$

where R_0 is the resistance at the reference temperature T_0, R is the resistance and temperature T. Figure 5A (lower left corner) shows the linear fit of the resistance versus the temperature, indicating a temperature sensitivity of 0.22 Ω K^{-1}.

The utilization of implantable strain sensors holds significant importance in monitoring the mechano-physiological functions of internal organs, including the abdominal region,[59] heart,[60−63] artery,[64] lung,[60] and urinary bladder.[60,65] In this context, we present our highly flexible strain sensor, featuring a SiC piezoresistive element measuring 300 μm × 450 μm, encapsulated between two layers of PI with a thickness of 4 μm. To assess strain sensitivity, we bonded the strain sensor to a one-side clamped acrylic beam (Figure S23A). Figure 7B (left) illustrates the sensor response when a 5 g weight is incrementally applied four times to the free end of the acrylic beam. The sensor effectively captures changes in strain within the acrylic beam under different loads, exhibiting excellent sensitivity and repeatability across three cycles. To further demonstrate repeatability, we applied loading and unloading of a 10 g weight through several cycles, showcasing the consistent and repeatable response signal of the sensor (Figure 7B-right). Employing FEA, we determine the strain on the acrylic beam and the position of the SiC electrode on the beam (Figure S23B). A gauge factor (G) of −11.1 is calculated using eq 7.

$$G = \frac{\Delta R}{\varepsilon R_0} \tag{7}$$

https://doi.org/10.1021/acsnano.4c15294
ACS Nano 2025, 19, 1642−1659

where ΔR is the resistance change caused by strain ε and R_0 is the resistance at undeformed mode. This strain gauge is in good agreement with a previous study[66] and is five times large than those typical metallic strain gauges.

Hysteresis is an important criterion to evaluate a sensor. We plot the relative resistance change of the temperature sensor and strain sensor in Figure S24. The hysteresis (H) is calculated as eq 8.

$$H = \frac{|A_{\text{loading}} - A_{\text{unloading}}|}{A_{\text{loading}}} \times 100\% \tag{8}$$

where A_{loading} and $A_{\text{unloading}}$ are the areas of the resistance change curves versus the strain or temperature, respectively.

The temperature sensor is laminated on a glass slide, which is attached to the surface of a hot plate. The temperature of the hot plate increased 50 °C each 30 min from 30 to 55 °C, and then decreased 5 °C after each 30 min until 30 °C. The semiconductor analyzer B1500 was employed to apply a constant voltage of 1 V and record the change in current of the sensor. The change of current of the sensor is shown in Figure S24A (left). Consequently, the hysteresis plot is shown in Figure S24A (right) with a hysteresis of 0.8%.

Relative change of resistance versus strain of a strain sensor is shown in Figure S24B (left), while Figure S24B (right) shows the long-term performance of a strain sensor. The hysteresis of the strain sensor in this paper is 51.6%. This high value of hysteresis is explained due to mismatch between mechanical properties of the adhesive layer used to bond the flexible thin film onto the acrylic plate with the plate. We validate our explanation by using the same experiment setup to a commercial strain gauge, which shows the hysteresis of 10.8%. A previous strain sensor of SiC material on a hard Si substrate was reported to have an extremely small hysteresis (0.91%),[67] which shows the stability of SiC material for strain sensing. The weak or irreversible adhesion interface of the sensing layer with the polymer substrate can contribute to the hysteresis behavior.[68−70]

Several efforts including employing modeling and control algorithm to compensate the creep and hysteresis effects of strain sensor have been proposed.[71,72] Previous studies also employed a constant temperature difference circuit, which contains a Wheatstone bridge and a feedback control circuit to compensate for temperature and strain.[73,74] Our previous work on the orientation dependence of the piezoresistive effect in 3C-SiC suggested that n-type 3C-SiC in the ⟨100⟩ orientation is highly sensitive to strain (with a gauge factor of −31), while n-type 3C-SiC in the ⟨110⟩ orientation shows a minimal gauge factor.[75,76] This phenomenon is relatively analogous to the most common cubic crystal semiconductor, silicon. Therefore, it is possible to compensate for thermal effects in strain sensing for SiC using design concepts that have been previously demonstrated in silicon, such as the rosette structure. In the Wheatstone bridge mentioned above, three constant resistors can be fabricated from n-type SiC ⟨110⟩, which are almost insensitive to strain, while the sensing element can be developed using n-type SiC ⟨100⟩ due to its large gauge factor. Since all four resistances are made from the same material, connecting them in a Wheatstone bridge circuit can mitigate the effects of temperature variation.

Moreover, we demonstrated the potential utility of our strain sensor for implantable applications through experiments with a blood artery phantom model. The experiment involved pressurizing a silicone tube with a 3 mm diameter by pumping water through a syringe, which simultaneously regulated the pressure within the tube. An entirely encapsulated strain sensor with a width of 1 mm and a thickness of 8 μm was affixed around the tube using epoxy (Figure S25A, inset). Employing small strain sensors minimizes invasiveness in the body. We subjected the system to pressurization at 1 bar and subsequent depressurization over 20 s intervals. Figure S25B further illustrates the potential of the strain sensors in measuring blood artery pressure, underscoring its utilization in physiological monitoring. As the pressure inside the tube increases, the tube wall expands, inducing a strain in the outer wall of the tube, which increases the electrical current in the strain sensor.

Impedance sensors have been used widely in monitoring health conditions such as cancer detection.[77−79] The integration of impedance sensors with soft robots for tumor identification shows promising possibility for timely detection of abnormal tissues.[80−82] Employing the wide optical bandgap of SiC, we present a transparent and durable sensor that can be attached onto soft robots for on-site tissue impedance measurement. The electrical impedance sensor consists of a pair of SiC electrodes, each measuring 300 × 450 μm and encapsulated between two layers of 4 μm PI. Open windows of 160 μm × 160 μm are positioned at the center of each electrode, while metal interconnects link the electrodes to the electrical circuit. An anisotropic poly(vinyl alcohol) (PVA) hydrogel serves as a tissue phantom model for impedance characterization, chosen for its physical properties resembling those of human tissues.[83] Our sensor not only exhibits excellent sensitivity and repeatability but also displays flexibility for integration onto the curved surface of a balloon catheter (Figure 7C, right) or the tips of a soft medical robot. The optical transparency of the electrode, which was proved in previous studies,[36,38] facilitates simultaneous impedance sensing and observation through micro cameras. The stable current−voltage characteristic of the SiC electrode, presented in Figure S26, under dark and light illumination conditions, indicates a consistent signal in environments both with and without light. In Figure 7C (left), a distinct contrast in impedance readings is observed between our sensor with and without the PVA hydrogel across a frequency range from 10 Hz to 1 MHz. The repeatability of SiC impedance sensors was confirmed through several touching and nontouching cycles with the PVA hydrogel at a frequency of 1 kHz, as depicted in Figure 7C (middle).

CONCLUSIONS

This work introduces SiC MEA as a versatile platform for multiplexed sensing, recording, and stimulation. Our unique technique combines backside lithography and transfer printing to increase the number of electrodes to enhance resolution and efficiency. Sandwiching the functional layers between two equivalent PI films significantly reduces strain levels significantly. We demonstrated the multimodalities in our SiC MEA for measuring temperature, strain, and tissue impedance as well as stimulating and recording biopotentials. These capabilities together with the optical transparency of SiC represent promising features for coupling of the electrical measurement and optical mapping.

While this work demonstrates the pacing function in cardiac tissues, the potential of SiC MEA can be extended beyond the applications of the heart, encompassing further utilization, such as neuromodulation and pain reduction. Notably, the

https://doi.org/10.1021/acsnano.4c15294
ACS Nano 2025, 19, 1642−1659

hydrolysis study on the durability of the SiC electrode under biofluid environments further ensures a prolonged operational lifespan.

It is noteworthy that the electrochemical performance of the SiC electrode presented in this study is relatively lower than that of commonly used materials for stimulation and recording such as Pt. This limitation can be overcome using different approaches that have been used in other material systems. For instance, a previous study by Rogers group showed that the perimeter of Au electrodes used for defibrillators can be increased by 36 times when employing a fractal shape design compared to the circular one, significantly increasing the total number of charges for stimulation.[28,84] A similar approach can be applied to SiC electrode by increasing the perimeter of the electrode without increasing geometry surface area. For example, our previous paper demonstrated the feasibility of creating a patterned fractal structure of SiC using the double-sided photolithography technique.[37] These structures can increase the perimeter of the electrode while still maintaining the flexibility of the electrode without increasing the physical surface area.[28,85,86]

Another potential approach involves increasing the doping density[87] or surface modifications of refs 87−92. These surface modification and doping approaches have been applied to conductive diamond, another transparent WBG material for long-term bioimplant. For instance, a boron-doped, highly nanostructured diamond showed a CSC_c of 10 mC/cm^2, which is comparable to the value reported for PEDOT.[93] Therefore, increasing the doping level (currently from 1019 cm^{-3}) to 1020 cm^{-3} could reduce the serial resistance and increase charge carrier density. The flat surface area of SiC (200 nm thick film) can be further engineered using a top-down fabrication technique. For instance, implementation of electron beam lithography can increase a high density of porous array with pore size less than 50 nm,[94] thereby significantly increasing the surface areas. This method can be applied to our SiC films, where the top 100 nm layer can be used to create a top-down porous electrode, while the bottom 100 nm serves as the biobarrier, as shown in Figure S27. The feasibility of using nanostructured surfaces to enhance the performance of SiC neural electrodes has been demonstrated in recent work from the Tian Research Group.[95] The authors employed a laser engraving technique to form two-dimensional (2D) SiC electrodes that can be used for cardiac pacing (tested on rat models), suggesting a promising possibility to boost the electrochemical performance of SiC through surface engineering.

While nanothin metals are not highly suitable for long-term stimulation, they can be employed in recording applications, as electrodes are exposed to relatively low biopotential (e.g., few tens to hundreds of micro-Volts). In this regard, a hybrid system of porous metal and thin film SiC could be a promising solution for chronic neurological recording applications. For example, we combined the low impedance porous metal with the inertness of SiC in our previous work for neurological recording.[3]

METHOD

Device Fabrication. To fabricate free-standing SiC membranes, we deposited 200 nm SiC layers by using low-pressure chemical vapor deposition on both sides of a silicon wafer to alleviate thermal stress during the growth process. The fabrication of SiC free-standing membranes began by patterning photoresist windows on one side of the wafer through a standard photolithography process. The SiC windows were then completely removed by using inductively coupled plasma, exposing the Si layer for subsequent KOH etching. After removal of the bulk Si layer, an RCA2 process effectively cleaned any residue contamination. The detailed fabrication process is provided in Supporting Information Note S1.

Hydrolysis Test. The glass substrates coated with SiC underwent Ti sputtering on both ends, leaving SiC exposed between the Ti electrodes to establish electrical contacts. Subsequently, the samples were immersed in 1× PBS solution and the alterations in the electrical resistance of SiC were monitored at regular intervals, initially every 24 h for the first week and later extended to a month. During the measurement process, the samples were taken from the PBS solution and rinsed with DI water before and after the measurements. Following each measurement, the electrodes were returned to a freshly prepared PBS solution and left undisturbed.

Biocompatibility Test. The biocompatibility assay was assessed by culturing fibroblast cells NIH/3T3 on the SiC membranes using a complete culture medium. Dulbecco's modified Eagle medium supplemented with 10% fetal bovine serum and 1% penicillin−streptomycin was used to prepare medium for NIH/3T3 cell culture. NIH/3T3 cells were cultured for 24, 48, and 96 h on SiC membranes, and the cell viability was then determined by MTT assay. NIH/3T3 cells cultured on a 96-well plate were set as a growth control, while dead cells on SiC membranes were used as a death control.

Theoretical Calculation and FEA for Mechanical Performance of Mesostructure. We use the following parameters for theoretical calculations and the FEA: EPI = 2.5 GPa, υPI = 0.34, ESiC = 330 GPa, υSiC = 0.28, EAl = 68.9 GPa, υAl = 0.34, where E and υ are elastic modulus and Poisson's ratio of the material, respectively. All theoretical equations are provided in the main text.

FEA for bending of thin films was conducted using the commercial software Abaqus. The thin film was modeled using four-node shell elements (S4R). Mesh refinement (23,000−25,000 elements) was conducted to ensure computational accuracy.

The FEA of acrylic beam was conducted by using ANSYS R2023. Linear elastic material properties of acrylic were assumed by considering small displacement and small strain phenomena. The following parameters were employed for the simulation:[96] E acrylic = 3.17 GPa, υ acrylic = 0.4.

Electrical Measurement. To characterize the fracture occurring in a thin film after bending, the thin film was contacted from a function generator (TENAMA 72-3555) to an oscilloscope (Rohde & Swharz RIB200h) as an active signal line. A sinusoidal wave was generated from the function generator to go through the thin film to the oscilloscope to see if there any change of the signal received in the oscilloscope.

The TCR can be calculated as

$$\mathrm{TCR} = \frac{\Delta R}{R}\frac{1}{\Delta T} \tag{9}$$

where ΔR is the change in resistance caused by the change ΔR in temperature and R is the resistance at reference temperature.

To record the electrical current of the devices, we use semiconductor analyzer B1500, while the LCR meter (Hiroki IM 3536) was used to characterize the impedance sensor. The PVA hydrogel was prepared by slowly adding PVA powder

https://doi.org/10.1021/acsnano.4c15294
ACS Nano 2025, 19, 1642−1659

(Sigma, Mw 146,000−186,000) into deionized (DI) water at a temperature of 85 °C while stirring vigorously until a viscous and clear solution was obtained. After the above solution cooled down, it was introduced into a Petri dish and frozen at −25° for 9 h and then thawed at room temperature for 5 h. Repeating the above freezing-thawing process 3 times yielded the PVA hydrogel.

To ensure the accuracy of the pressure level in the silicone tube for blood pressure monitoring experiments, we use a step motor attached to the syringe to control the level of water delivered into the tube.

The electrochemical impedance and CV were measured using a potentiostat VSP-300 workstation. An Ag/AgCl electrode was used as the reference electrode, while a Pt electrode was sued as the return electrode. The experiment was conducted using a PBS 1× solution.

Ex Vivo Experiments. Upon completion of electrochemical characterization, the "material name" electrodes were evaluated ex vivo using a sinoatrial node and surrounding right atrial pectinate muscle tissue preparation obtained from the heart of a New Zealand White rabbit (tissue sharing arrangement, UNSW Animal Care and Ethics Committee approval 22/101A). The spontaneously beating tissue was maintained by superfusing with Krebs-Ringer solution and mounted in a recording chamber, gassed with carbogen (95% O_2, 5% CO_2), and circulated at a rate of ≈4 mL/min by two MP-II Mini peristaltic pumps (Harvard Apparatus, USA). The temperature of the solution was monitored and maintained at 34 °C using a TC-324B temperature controller (Warner Instruments, USA). Bipolar cardiac electrograms were captured through an in-house-fabricated tungsten electrode in reference to an Ag−AgCl ground pellet placed distally in the recording chamber. Signals from the electrodes were transmitted to a standard bioamplifier (CardioPhys, gain 100, 0.1 Hz−10 kHz). The array was placed onto a flat portion of the tissue, and stimulation was conducted using one pair of driving electrodes at a time. Monophasic stimulus pulses (4 Hz frequency, 10 ms pulse width) were driven by an analog output from a PowerLab35/4 system (ADInstruments, USA). The stimulus intensity varied from 1 to 7 V. A prestimulus baseline of 10 s and a poststimulus baseline of 10 s were recorded for each intensity.

In Vivo Experiment. *Animal and Housing.* Four adult mice, averaging 50 ± 10 g in body weight, were utilized for this study. All experimental protocols were approved by the University's Animal Research Ethics Committee (Protocol number: NRS/01/24/AEC). The mice were individually housed in separate cages and had ad libitum access to in-house-prepared pelleted feed and filtered water throughout the study.

Surgical Procedure. All animals received Buprenorphine (0.05 mg/kg) 30 min before surgery to provide preoperative analgesia. Anesthesia was induced and maintained with isoflurane (3−5% for induction and 1−1.5% for maintenance in oxygen at 1 L/min flow rate) delivered via a standard anesthetic machine. The control and SiC films were sterilized with 70% ethanol and rinsed in sterile normal saline before implantation.

The procedure was conducted under sterile conditions. The implantation area on the dorsal side of each mouse was shaved and disinfected with povidone-iodine and surgical spirit. A sterile surgical blade made two approximately 1.5 cm long sagittal incisions. The underlying connective tissue was bluntly dissected to create a subcutaneous pocket. A 10 mm × 10 mm sterile SiC film was placed in the right dorsal pocket, while a 10 mm × 10 mm sterile control film was positioned on the left dorsal side (see Figure 5, right), using micro forceps for precise placement.

The skin incisions were closed with interrupted 5−0 silk sutures. The surgical site was then cleansed with sterile saline to remove the blood and debris. Postoperative analgesia (Buprenorphine, 0.05 mg/kg) was administered for 48 h postoperatively according to the approved guidelines. For wound care, topical ointment Savlon (Chlorhexidine Hydrochloride 1 mg/g and Cetrimide 5 mg/g) was applied prophylactically to prevent infection.

One-week postimplantation, the animals were euthanized by gradual CO_2 inhalation, with the absence of corneal reflex and response to paw pinch confirming death. The tissues around the implants were harvested *en bloc*, immersion-fixed in 4% neutral buffered paraformaldehyde for 24 h, and then stored at 4 °C. Following fixation, tissues were cryoprotected in 30% sucrose, embedded in an optimal cutting temperature medium, and sectioned at 20 μm thickness at −20 °C.

Histopathological Evaluation. Macroscopic Evaluation. Photographs of the film-tissue interface were taken, and a semiquantitative morphological analysis was conducted. Any signs of poor biocompatibility, such as acute inflammation, purulent exudate, localized necrosis, and implant rejection, were noted. The extent of implant extrusion was also evaluated.

Microscopic Evaluation. For histological analysis, 20 μm sections were cut with a cryostat, mounted on glass slides, and stained with hematoxylin and eosin (H&E). Tissue response was evaluated using light microscopy, focusing on inflammatory responses and morphological changes around the implanted films.

ASSOCIATED CONTENT

Supporting Information

The Supporting Information is available free of charge at https://pubs.acs.org/doi/10.1021/acsnano.4c15294.

Detailed fabrication methods and various designs and structures of the bioelectronic interface; additional information on FEA, electrode chemistry characterization, and the experimental setup, along with results from the ex vivo cardiac tissue pacing tests; further details and results for electronic sensing tests; and comparison of different types of SiC materials for implantable applications (PDF)

Helium leak test on SiC nanomembranes (MP4)

AUTHOR INFORMATION

Corresponding Author

Hoang-Phuong Phan − *School of Mechanical and Manufacturing Engineering, University of New South Wales, Sydney, New South Wales 2052, Australia; Tyree Foundation Institute of Health Engineering, University of New South Wales, Sydney, New South Wales 2052, Australia;* orcid.org/0000-0002-1724-5667; Email: hp.phan@unsw.edu.au

https://doi.org/10.1021/acsnano.4c15294
ACS Nano 2025, 19, 1642−1659

Authors

Thanh An Truong − *School of Mechanical and Manufacturing Engineering, University of New South Wales, Sydney, New South Wales 2052, Australia*

Xinghao Huang − *Department of Aerospace and Mechanical Engineering, University of Southern California, Los Angeles, California 90089, United States*

Matthew Barton − *School of Nursing & Midwifery, Griffith University, Gold Coast Campus, Queensland 4215, Australia; Institute for Biomedicine and Glycomics, Griffith University, Gold Coast Campus, Queensland 4215, Australia; Clem Jones Centre for Neurobiology and Stem Cell Research, Griffith University, Nathan, Queensland 4111, Australia*

Aditya Ashok − *School of Mechanical and Manufacturing Engineering, University of New South Wales, Sydney, New South Wales 2052, Australia;* orcid.org/0000-0003-0479-0348

Amr Al Abed − *Graduate School of Biomedical Engineering, University of New South Wales, Sydney, New South Wales 2052, Australia*

Reem Almasri − *Graduate School of Biomedical Engineering, University of New South Wales, Sydney, New South Wales 2052, Australia*

Mohit N. Shivdasanic − *Graduate School of Biomedical Engineering, University of New South Wales, Sydney, New South Wales 2052, Australia*

Ronak Reshamwala − *Institute for Biomedicine and Glycomics, Griffith University, Gold Coast Campus, Queensland 4215, Australia; Clem Jones Centre for Neurobiology and Stem Cell Research, Griffith University, Nathan, Queensland 4111, Australia*

Joshua Ingles − *Institute for Biomedicine and Glycomics, Griffith University, Gold Coast Campus, Queensland 4215, Australia; Clem Jones Centre for Neurobiology and Stem Cell Research, Griffith University, Nathan, Queensland 4111, Australia*

Mai Thanh Thai − *Graduate School of Biomedical Engineering, University of New South Wales, Sydney, New South Wales 2052, Australia; College of Engineering and Computer Science and VinUni-Illinois Smart Health Center, Vin University, Hanoi 100000, Vietnam*

Chi Cong Nguyen − *Graduate School of Biomedical Engineering, University of New South Wales, Sydney, New South Wales 2052, Australia*

Sinuo Zhao − *School of Mechanical and Manufacturing Engineering, University of New South Wales, Sydney, New South Wales 2052, Australia*

Xiuwen Zhang − *School of Chemical Engineering, University of New South Wales, Sydney, New South Wales 2052, Australia*

Zi Gu − *School of Chemical Engineering, Australian Centre for Nanomedicine (ACN), and UNSW RNA Institute, University of New South Wales, Sydney, New South Wales 2052, Australia;* orcid.org/0000-0002-7153-6596

Arya Vasanth − *School of Mechanical and Manufacturing Engineering, University of New South Wales, Sydney, New South Wales 2052, Australia*

Shuhua Peng − *School of Mechanical and Manufacturing Engineering, University of New South Wales, Sydney, New South Wales 2052, Australia;* orcid.org/0000-0001-5680-9448

Tuan-Khoa Nguyen − *Queensland Micro and Nanotechnology Centre, Griffith University, Nathan Campus, Queensland 4111, Australia;* orcid.org/0000-0003-1271-9576

Nho Do − *Clem Jones Centre for Neurobiology and Stem Cell Research, Griffith University, Nathan, Queensland 4111, Australia; Tyree Foundation Institute of Health Engineering, University of New South Wales, Sydney, New South Wales 2052, Australia*

Nam-Trung Nguyen − *Queensland Micro and Nanotechnology Centre, Griffith University, Nathan Campus, Queensland 4111, Australia*

Hangbo Zhao − *Department of Aerospace and Mechanical Engineering, University of Southern California, Los Angeles, California 90089, United States; Alfred E. Mann Department of Biomedical Engineering, University of Southern California, Los Angeles, California 90089, United States;* orcid.org/0000-0001-5229-4192

Complete contact information is available at: https://pubs.acs.org/10.1021/acsnano.4c15294

Author Contributions

T.A.T. conceived and planned the research, assisted FEA, fabricated devices, conducted experiments, and wrote the manuscript. H.P.P. supervised the research and cowrote the manuscript. A.A. conducted hydrolysis test, assisted electrochemical measurements, and proofread the paper. X.H. and H.Z. performed the FEA, assisted the fabrication process development, and proofread the manuscript. T.K.N. and N.T.N. fabricated free-standing SiC membranes and proofread the manuscript. T.N.D. and M.T.T. assisted strain sensor characterization and proofread the manuscript. R.A. and A.A.A. assisted in the ex vivo experiment and wrote the manuscript. M.S. assisted in the electrochemical characterization and wrote the manuscript. X.W.Z. and Z.G. did the biocompatibility experiment and cowrote the paper. S.H.P. fabricated the PVA hydrogel and assisted in impedance sensor characterization. C.C.N. assisted in data collection and cowrote the paper. M.B., R.R., and J.I. conducted the in vivo experiment and cowrote the manuscript.

Funding

ARC DE240100408; DE200100238; DP230101312.

Notes

The authors declare no competing financial interest.

All experimental procedures were conducted in accordance with the Australian Code for the Care and Use of Animals for Scientific Purposes eighth Edition 2013 and were approved by the University of New South Wales Animal Care and Ethics Committee (22/101A).

ACKNOWLEDGMENTS

T.K.N. acknowledged support from ARC DE240100408. H.P.P. acknowledged funding from Australian Research Council (DP230101312, FT240100203). This work was performed in part at the NSW Node of the Australian National Fabrication Facility.

ABBREVIATIONS

MEA	multielectrode array
WBG	wide bandgap
NMP	neutral mechanical plane
ICD	cardioverter-defibrillator

PI	polyimide
PDMS	polydimethylsiloxane
PBS	phosphate buffered saline
PMMA	poly(methyl methacrylate)
FEA	finite element method

REFERENCES

(1) Heo, D. N.; Kim, H. J.; Lee, Y. J.; Heo, M.; Lee, S. J.; Lee, D.; Do, S. H.; Lee, S. H.; Kwon, I. K. Flexible and Highly Biocompatible Nanofiber-Based Electrodes for Neural Surface Interfacing. *ACS Nano* **2017**, *11* (3), 2961−2971.

(2) Wang, J.; Wang, T.; Liu, H.; Wang, K.; Moses, K.; Feng, Z.; Li, P.; Huang, W. Flexible Electrodes for Brain−Computer Interface System. *Adv. Mater.* **2023**, *35* (47), 2211012.

(3) Ashok, A.; Nguyen, T. K.; Barton, M.; Leitch, M.; Masud, M. K.; Park, H.; Truong, T. A.; Kaneti, Y. V.; Ta, H. T.; Li, X.; Liang, K.; Do, T. N.; Wang, C. H.; Nguyen, N. T.; Yamauchi, Y.; Phan, H. P. Flexible Nanoarchitectonics for Biosensing and Physiological Monitoring Applications. *Small* **2023**, *19* (9), 2204946.

(4) Zhao, E. T.; Hull, J. M.; Mintz Hemed, N.; Uluşan, H.; Bartram, J.; Zhang, A.; Wang, P.; Pham, A.; Ronchi, S.; Huguenard, J. R.; Hierlemann, A.; Melosh, N. A. A CMOS-Based Highly Scalable Flexible Neural Electrode Interface. *Sci. Adv.* **2023**, *9* (23), No. eadf9524.

(5) Sunwoo, S. H.; Cha, M. J.; Han, S. I.; Kang, H.; Cho, Y. S.; Yeom, D. H.; Park, C. S.; Park, N. K.; Choi, S. W.; Kim, S. J.; Cha, G. D.; Jung, D.; Choi, S.; Oh, S.; Nam, G. B.; Hyeon, T.; Kim, D. H.; Lee, S. P. Ventricular Tachyarrhythmia Treatment and Prevention by Subthreshold Stimulation with Stretchable Epicardial Multichannel Electrode Array. *Sci. Adv.* **2023**, *9* (13), No. eadf6856.

(6) Hwang, G. T.; Park, H.; Lee, J. H.; Oh, S.; Park, K. I.; Byun, M.; Park, H.; Ahn, G.; Jeong, C. K.; No, K.; Kwon, H.; Lee, S. G.; Joung, B.; Lee, K. J. Self-Powered Cardiac Pacemaker Enabled by Flexible Single Crystalline PMN-PT Piezoelectric Energy Harvester. *Adv. Mater.* **2014**, *26* (28), 4880−4887.

(7) Wang, S.; Cui, Q.; Abiri, P.; Roustaei, M.; Zhu, E.; Li, Y. R.; Wang, K.; Duarte, S.; Yang, L.; Ebrahimi, R.; Bersohn, M.; Chen, J.; Hsiai, T. K. A Self-Assembled Implantable Microtubular Pacemaker for Wireless Cardiac Electrotherapy. *Sci. Adv.* **2023**, *9* (42), No. eadj0540.

(8) Gutruf, P.; Yin, R. T.; Lee, K. B.; Ausra, J.; Brennan, J. A.; Qiao, Y.; Xie, Z.; Peralta, R.; Talarico, O.; Murillo, A.; Chen, S. W.; Leshock, J. P.; Haney, C. R.; Waters, E. A.; Zhang, C.; Luan, H.; Huang, Y.; Trachiotis, G.; Efimov, I. R.; Rogers, J. A. Wireless, Battery-Free, Fully Implantable Multimodal and Multisite Pacemakers for Applications in Small Animal Models. *Nat. Commun.* **2019**, *10* (1), 1−10.

(9) Chen, Z.; Lin, Z.; Obaid, S. N.; Rytkin, E.; George, S. A.; Bach, C.; Madrid, M.; Liu, M.; LaPiano, J.; Fehr, A.; Shi, X.; Quirion, N.; Russo, B.; Knight, H.; Aduwari, A.; Efimov, I. R.; Lu, L. Soft, Bioresorbable, Transparent Microelectrode Arrays for Multimodal Spatiotemporal Mapping and Modulation of Cardiac Physiology. *Sci. Adv.* **2023**, *9* (27), No. eadi0757.

(10) Ausra, J.; Madrid, M.; Yin, R. T.; Hanna, J.; Arnott, S.; Brennan, J. A.; Peralta, R.; Clausen, D.; Bakall, J. A.; Efimov, I. R.; Gutruf, P. Wireless Fully Implantable Cardiac Stimulation and Recording with on-Device Computation for Closed-Loop Pacing and Defibrillation. *Sci. Adv.* **2022**, *8* (43), 7469.

(11) Choi, Y. S.; Yin, R. T.; Pfenniger, A.; Koo, J.; Avila, R.; Benjamin Lee, K.; Chen, S. W.; Lee, G.; Li, G.; Qiao, Y.; Murillo-Berlioz, A.; Kiss, A.; Han, S.; Lee, S. M.; Li, C.; Xie, Z.; Chen, Y. Y.; Burrell, A.; Geist, B.; Jeong, H.; Kim, J.; Yoon, H. J.; Banks, A.; Kang, S. K.; Zhang, Z. J.; Haney, C. R.; Sahakian, A. V.; Johnson, D.; Efimova, T.; Huang, Y.; Trachiotis, G. D.; Knight, B. P.; Arora, R. K.; Efimov, I. R.; Rogers, J. A. Fully Implantable and Bioresorbable Cardiac Pacemakers without Leads or Batteries. *Nat. Biotechnol.* **2021**, *39* (10), 1228−1238.

(12) Viventi, J.; Kim, D. H.; Vigeland, L.; Frechette, E. S.; Blanco, J. A.; Kim, Y. S.; Avrin, A. E.; Tiruvadi, V. R.; Hwang, S. W.; Vanleer, A. C.; Wulsin, D. F.; Davis, K.; Gelber, C. E.; Palmer, L.; Van Der Spiegel, J.; Wu, J.; Xiao, J.; Huang, Y.; Contreras, D.; Rogers, J. A.; Litt, B. Flexible, Foldable, Actively Multiplexed, High-Density Electrode Array for Mapping Brain Activity In Vivo. *Nat. Neurosci.* **2011**, *14* (12), 1599.

(13) Sang, M.; Kim, K.; Shin, J.; Yu, K. J. Ultra-Thin Flexible Encapsulating Materials for Soft Bio-Integrated Electronics. *Adv. Sci.* **2022**, *9* (30), 2202980.

(14) Gillberg, J. Detection of Cardiac Tachyarrhythmias in Implantable Devices. *J. Electrocardiol.* **2007**, *40* (6), S123−S128.

(15) Rao, A.; Bennett, S. Cardiac Implantable Electronic Devices: An Overview for Primary Care. *Br. J. Gen. Pract.* **2022**, *72* (721), 402−404.

(16) Abraham, W. T.; Stough, W. G.; Piña, I. L.; Linde, C.; Borer, J. S.; De Ferrari, G. M.; Mehran, R.; Stein, K. M.; Vincent, A.; Yadav, J. S.; Anker, S. D.; Zannad, F. Trials of Implantable Monitoring Devices in Heart Failure: Which Design Is Optimal? *Nat. Rev. Cardiol.* **2014**, *11* (10), 576−585.

(17) Volterrani, M.; Spoletini, I.; Angermann, C.; Rosano, G.; Coats, A. J. Implantable Devices for Heart Failure Monitoring: The CardioMEMS System. *Eur. Hear. J. Suppl.* **2019**, *21* (Supplement_M), M50−M53.

(18) Udo, E. O.; Zuithoff, N. P. A.; Van Hemel, N. M.; De Cock, C. C.; Hendriks, T.; Doevendans, P. A.; Moons, K. G. M. Incidence and Predictors of Short- and Long-Term Complications in Pacemaker Therapy: The FOLLOWPACE Study. *Heart Rhythm* **2012**, *9* (5), 728−735.

(19) Sunwoo, S.-H.; Han, S. I.; Park, C. S.; Kim, J. H.; Georgiou, J. S.; Lee, S.-P.; Kim, D.-H.; Hyeon, T. Soft Bioelectronics for the Management of Cardiovascular Diseases. *Nat. Rev. Bioeng.* **2023**, *2*, 8−24.

(20) Xu, X.; Chen, Y.; He, P.; Wang, S.; Ling, K.; Liu, L.; Lei, P.; Huang, X.; Zhao, H.; Cao, J.; Yang, J. Wearable CNT/Ti3C2Tx MXene/PDMS Composite Strain Sensor with Enhanced Stability for Real-Time Human Healthcare Monitoring. *Nano Res.* **2021**, *14* (8), 2875−2883.

(21) Bang, J.; Chun, B.; Lim, J.; Han, Y.; So, H. Ultra-Broad Linear Range and Sensitive Flexible Piezoresistive Sensor Using Reversed Lattice Structure for Wearable Electronics. *ACS Appl. Mater. Interfaces* **2023**, *15* (28), 34120−34131.

(22) Tanusha, D.; Badhulika, S. Comparative Analysis of Micro Patterned PDMS-Based Piezoresistive Pressure Sensors with Multi-functional Strain and Health Monitoring Applications. *Sens. Actuators, A* **2024**, *369*, 115139.

(23) Lee, J.; So, H. 3D-Printing-Assisted Flexible Pressure Sensor with a Concentric Circle Pattern and High Sensitivity for Health Monitoring. *Microsyst. Nanoeng.* **2023**, *9* (1), 1−12.

(24) Sharma, P.; Sharma, R.; Janyani, V.; Verma, D. Development of a Multi-Modal Graphene Nanoparticles (GNP)- Polydimethylsiloxane (PDMS) Flexible Sensor for Human Activity Monitoring and Health Assessment. *Int. J. Electrochem. Sci.* **2023**, *18* (9), 100236.

(25) Tang, T.; Liu, X.; Yuan, Y.; Zhang, T.; Kiya, R.; Yang, Y.; Suzuki, K.; Tanaka, Y.; Li, M.; Hosokawa, Y.; Yalikun, Y. Assessment of the Electrical Penetration of Cell Membranes Using Four-Frequency Impedance Cytometry. *Microsyst. Nanoeng.* **2022**, *8* (1), 1−12.

(26) Viventi, J.; Kim, D. H.; Moss, J. D.; Kim, Y. S.; Blanco, J. A.; Annetta, N.; Hicks, A.; Xiao, J.; Huang, Y.; Callans, D. J.; Rogers, J. A.; Litt, B. A Conformal, Bio-Interfaced Class of Silicon Electronics for Mapping Cardiac Electrophysiology. *Sci. Transl. Med.* **2010**, *2* (24), 24ra22.

(27) Park, J.; Choi, S.; Janardhan, A. H.; Lee, S. Y.; Raut, S.; Soares, J.; Shin, K.; Yang, S.; Lee, C.; Kang, K. W.; Cho, H. R.; Kim, S. J.; Seo, P.; Hyun, W.; Jung, S.; Lee, H. J.; Lee, N.; Choi, S. H.; Sacks, M.; Lu, N.; Josephson, M. E.; Hyeon, T.; Kim, D. H.; Hwang, H. J. Electromechanical Cardioplasty Using a Wrapped Elasto-Conductive Epicardial Mesh. *Sci. Transl. Med.* **2016**, *8* (344), 344ra86.

https://doi.org/10.1021/acsnano.4c15294
ACS Nano 2025, 19, 1642−1659

(28) Xu, L.; Gutbrod, S. R.; Ma, Y.; Petrossians, A.; Liu, Y.; Webb, R. C.; Fan, J. A.; Yang, Z.; Xu, R.; Whalen, J. J., III; Weiland, J. D.; Huang, Y.; Efimov, I. R.; Rogers, J. A. Materials and Fractal Designs for 3D Multifunctional Integumentary Membranes with Capabilities in Cardiac Electrotherapy. *Adv. Mater.* **2015**, *27* (10), 1731−1737.
(29) Fang, H.; Yu, K. J.; Gloschat, C.; Yang, Z.; Song, E.; Chiang, C. H.; Zhao, J.; Won, S. M.; Xu, S.; Trumpis, M.; Zhong, Y.; Han, S. W.; Xue, Y.; Xu, D.; Choi, S. W.; Cauwenberghs, G.; Kay, M.; Huang, Y.; Viventi, J.; Efimov, I. R.; Rogers, J. A. Capacitively Coupled Arrays of Multiplexed Flexible Silicon Transistors for Long-Term Cardiac Electrophysiology. *Nat. Biomed. Eng.* **2017**, *1* (3), 1−12.
(30) Hejazi, M. A.; Tong, W.; Stacey, A.; Soto-Breceda, A.; Ibbotson, M. R.; Yunzab, M.; Maturana, M. I.; Almasi, A.; Jung, Y. J.; Sun, S.; Meffin, H.; Fang, J.; Stamp, M. E. M.; Ganesan, K.; Fox, K.; Rifai, A.; Nadarajah, A.; Falahatdoost, S.; Prawer, S.; Apollo, N. V.; Garrett, D. J. Hybrid Diamond/Carbon Fiber Microelectrodes Enable Multimodal Electrical/Chemical Neural Interfacing. *Biomaterials* **2020**, *230*, 119648.
(31) Nguyen, N. K.; Nguyen, T.; Nguyen, T. K.; Yadav, S.; Dinh, T.; Masud, M. K.; Singha, P.; Do, T. N.; Barton, M. J.; Ta, H. T.; Kashaninejad, N.; Ooi, C. H.; Nguyen, N. T.; Phan, H. P. Wide-Band-Gap Semiconductors for Biointegrated Electronics: Recent Advances and Future Directions. *ACS Appl. Electron. Mater.* **2021**, *3* (5), 1959−1981.
(32) Diaz-Botia, C. A.; Luna, L. E.; Neely, R. M.; Chamanzar, M.; Carraro, C.; Carmena, J. M.; Sabes, P. N.; Maboudian, R.; Maharbiz, M. M. A Silicon Carbide Array for Electrocorticography and Peripheral Nerve Recording. *J. Neural. Eng.* **2017**, *14* (5), 056006.
(33) Deku, F.; Cohen, Y.; Joshi-Imre, A.; Kanneganti, A.; Gardner, T. J.; Cogan, S. F. Amorphous Silicon Carbide Ultramicroelectrode Arrays for Neural Stimulation and Recording. *J. Neural. Eng.* **2018**, *15* (1), 016007.
(34) Greenhorn, S.; Bano, E.; Stambouli, V.; Zekentes, K. Amorphous SiC Thin Films Deposited by Plasma-Enhanced Chemical Vapor Deposition for Passivation in Biomedical Devices. *Materials* **2024**, *17* (5), 1135.
(35) Dinh, T.; Dao, D. V.; Phan, H. P.; Wang, L.; Qamar, A.; Nguyen, N. T.; Tanner, P.; Rybachuk, M. Charge Transport and Activation Energy of Amorphous Silicon Carbide Thin Film on Quartz at Elevated Temperature. *Appl. Phys. Express* **2015**, *8* (6), 061303.
(36) Phan, H. P.; Zhong, Y.; Nguyen, T. K.; Park, Y.; Dinh, T.; Song, E.; Vadivelu, R. K.; Masud, M. K.; Li, J.; Shiddiky, M. J. A.; Dao, D.; Yamauchi, Y.; Rogers, J. A.; Nguyen, N. T. Long-Lived, Transferred Crystalline Silicon Carbide Nanomembranes for Implantable Flexible Electronics. *ACS Nano* **2019**, *13* (10), 11572−11581.
(37) Truong, T. A.; Nguyen, T. K.; Huang, X.; Ashok, A.; Yadav, S.; Park, Y.; Thai, M. T.; Nguyen, N. K.; Fallahi, H.; Peng, S.; Dimitrijev, S.; Toh, Y. C.; Yamauchi, Y.; Wang, C. H.; Lovell, N. H.; Rogers, J. A.; Do, T. N.; Nguyen, N. T.; Zhao, H.; Phan, H. P. Engineering Route for Stretchable, 3D Microarchitectures of Wide Bandgap Semiconductors for Biomedical Applications. *Adv. Funct. Mater.* **2023**, *33* (34), 2211781.
(38) Pham, T.-A.; Nguyen, T.-K.; Vadivelu, R. K.; Dinh, T.; Qamar, A.; Yadav, S.; Yamauchi, Y.; Rogers, J. A.; Nguyen, N.-T.; Phan, H.-P. A Versatile Sacrificial Layer for Transfer Printing of Wide Bandgap Materials for Implantable and Stretchable Bioelectronics. *Adv. Funct. Mater.* **2020**, *30* (43), 2004655.
(39) Cho, Y. U.; Lim, S. L.; Hong, J. H.; Yu, K. J. Transparent Neural Implantable Devices: A Comprehensive Review of Challenges and Progress. *npj Flexible Electron.* **2022**, *6* (1), 1−18.
(40) Nguyen, T. K.; Barton, M.; Ashok, A.; Truong, T. A.; Yadav, S.; Leitch, M.; Nguyen, T. V.; Kashaninejad, N.; Dinh, T.; Hold, L.; Yamauchi, Y.; Nguyen, N. T.; Phan, H. P. Wide Bandgap Semiconductor Nanomembranes as a Long-Term Biointerface for Flexible, Implanted Neuromodulator. *Proc. Natl. Acad. Sci. U.S.A.* **2022**, *119* (33), No. e2203287119.
(41) Widlund, T.; Yang, S.; Hsu, Y. Y.; Lu, N. Stretchability and Compliance of Freestanding Serpentine-Shaped Ribbons. *Int. J. Solids Struct.* **2014**, *51* (23−24), 4026−4037.
(42) Kim, D.-H.; Wang, S.; Keum, H.; Ghaffari, R.; Kim, Y.-S.; Tao, H.; Panilaitis, B.; Li, M.; Kang, Z.; Omenetto, F.; Huang, Y.; Rogers, J. A. Thin Flexible Sensors and Actuators as "Instrumented" Surgical Sutures for Targeted Wound Monitoring and Therapy. *Small* **2012**, *8* (21), 3263−3268.
(43) Song, E.; Li, J.; Won, S. M.; Bai, W.; Rogers, J. A. Materials for Flexible Bioelectronic Systems as Chronic Neural Interfaces. *Nat. Mater.* **2020**, *19* (6), 590−603.
(44) Jackson, K. M.; Dunning, J.; Zorman, C. A.; Mehregany, M.; Sharpe, W. N. Mechanical Properties of Epitaxial 3C Silicon Carbide Thin Films. *J. Microelectromech. Syst.* **2005**, *14* (4), 664−672.
(45) Jackson, K. M.; Edwards, R. L.; Dirras, G. F.; Sharpe, W. N. Mechanical Properties of Thin Film Silicon Carbide. *MRS Online Proc. Libr.* **2001**, *687*, B6.3.
(46) Ogawa, H.; Suzuki, K.; Kaneko, S.; Nakano, Y.; Ishikawa, Y.; Kitahara, T. Tensile Testing of Microfabricated Thin Films. *Microsyst. Technol.* **1997**, *3* (3), 117−121.
(47) Hammer, N.; Glätzner, J.; Feja, C.; Kühne, C.; Meixensberger, J.; Planitzer, U.; Schleifenbaum, S.; Tillmann, B. N.; Winkler, D. Human Vagus Nerve Branching in the Cervical Region. *PLoS One* **2015**, *10* (2), No. e0118006.
(48) Jenny, C.; van der Linde, J.; Hundsberger, T.; Broser, P. J. Correlation between Age and the Sciatic Nerve Diameter in the First 2 Years of Life: A High-Resolution Ultrasound Study. *Brain Behav.* **2023**, *13* (4), No. e2944.
(49) Solanki, G. A.; Lo, W. B.; Hendriksz, C. J. MRI Morphometric Characterisation of the Paediatric Cervical Spine and Spinal Cord in Children with MPS IVA (Morquio-Brailsford Syndrome). *J. Inherit. Metab. Dis.* **2013**, *36* (2), 329.
(50) Hammer, N.; Löffler, S.; Cakmak, Y. O.; Ondruschka, B.; Planitzer, U.; Schultz, M.; Winkler, D.; Weise, D. Cervical Vagus Nerve Morphometry and Vascularity in the Context of Nerve Stimulation—A Cadaveric Study. *Sci. Rep.* **2018**, *8* (1), 7997.
(51) Cannata, G.; Pezzato, S.; Esposito, S.; Moscatelli, A. Optic Nerve Sheath Diameter Ultrasound: A Non-Invasive Approach to Evaluate Increased Intracranial Pressure in Critically Ill Pediatric Patients. *Diagnostics* **2022**, *12* (3), 767.
(52) Schulte-Fischedick, J.; Zern, A.; Mayer, J.; Rühle, M.; Frieß, M.; Krenkel, W.; Kochendörfer, R. The Morphology of Silicon Carbide in C/C−SiC Composites. *Mater. Sci. Eng., A* **2002**, *332* (1−2), 146−152.
(53) Brannon, R. M.; Lee, M. Y.; Bronowski, D. R. *Uniaxial and Triaxial Compression Tests of Silicon Carbide Ceramics under Quasi-Static Loading Condition*, 2005. .
(54) Garrett, D. J.; Ganesan, K.; Stacey, A.; Fox, K.; Meffin, H.; Prawer, S. Ultra-Nanocrystalline Diamond Electrodes: Optimization towards Neural Stimulation Applications. *J. Neural. Eng.* **2012**, *9* (1), 016002.
(55) Ganesan, K.; Garrett, D. J.; Ahnood, A.; Shivdasani, M. N.; Tong, W.; Turnley, A. M.; Fox, K.; Meffin, H.; Prawer, S. An All-Diamond, Hermetic Electrical Feedthrough Array for a Retinal Prosthesis. *Biomaterials* **2014**, *35* (3), 908−915.
(56) Cogan, S. F. Neural Stimulation and Recording Electrodes. *Annu. Rev. Biomed. Eng.* **2008**, *10*, 275−309.
(57) Lu, D.; Li, S.; Yang, Q.; Arafa, H. M.; Xu, Y.; Yan, Y.; Ostojich, D.; Bai, W.; Guo, H.; Wu, C.; Li, S.; Jacobson, L.; Westman, A. M.; MacEwan, M. R.; Huang, Y.; Pet, M.; Rogers, J. A. Implantable, Wireless, Self-Fixing Thermal Sensors for Continuous Measurements of Microvascular Blood Flow in Flaps and Organ Grafts. *Biosens. Bioelectron.* **2022**, *206*, 114145.
(58) Madhvapathy, S. R.; Wang, J. J.; Wang, H.; Patel, M.; Chang, A.; Zheng, X.; Huang, Y.; Zhang, Z. J.; Gallon, L.; Rogers, J. A. Implantable Bioelectronic Systems for Early Detection of Kidney Transplant Rejection. *Science* **2023**, *381* (6662), 1105−1112.
(59) Jiang, H.; Carter, N. M.; Zareei, A.; Nejati, S.; Waimin, J. F.; Chittiboyina, S.; Niedert, E. E.; Soleimani, T.; Lelièvre, S. A.;

Goergen, C. J.; Rahimi, R. A Wireless Implantable Strain Sensing Scheme Using Ultrasound Imaging of Highly Stretchable Zinc Oxide/Poly Dimethylacrylamide Nanocomposite Hydrogel. *ACS Appl. Bio Mater.* **2020**, *3* (7), 4012−4024.
(60) Ryu, B.; Kim, C. Y.; Park, S. P.; Lee, K. Y.; Lee, S. In Vivo Implantable Strain Sensor for Real-Time and Precise Pathophysiological Monitoring of Contractile Living Organs. *Adv. Funct. Mater.* **2023**, *33* (44), 2305769.
(61) Zou, L.; Chen, X.; Servati, A.; Soltanian, S.; Servati, P.; Wang, Z. J. A Blind Source Separation Framework for Monitoring Heart Beat Rate Using Nanofiber-Based Strain Sensors. *IEEE Sens. J.* **2016**, *16* (3), 762−772.
(62) Dual, S. A.; Llerena Zambrano, B.; Sündermann, S.; Cesarovic, N.; Kron, M.; Magkoutas, K.; Hengsteler, J.; Falk, V.; Starck, C.; Meboldt, M.; Vörös, J.; Schmid Daners, M. Continuous Heart Volume Monitoring by Fully Implantable Soft Strain Sensor. *Adv. Healthcare Mater.* **2020**, *9* (19), 2000855.
(63) Kwon, K.; Kim, J. U.; Won, S. M.; Zhao, J.; Avila, R.; Wang, H.; Chun, K. S.; Jang, H.; Lee, K. H.; Kim, J. H.; Yoo, S.; Kang, Y. J.; Kim, J.; Lim, J.; Park, Y.; Lu, W.; Kim, T. i.; Banks, A.; Huang, Y.; Rogers, J. A. A Battery-Less Wireless Implant for the Continuous Monitoring of Vascular Pressure, Flow Rate and Temperature. *Nat. Biomed. Eng.* **2023**, *7* (10), 1215−1228.
(64) Boutry, C. M.; Beker, L.; Kaizawa, Y.; Vassos, C.; Tran, H.; Hinckley, A. C.; Pfattner, R.; Niu, S.; Li, J.; Claverie, J.; Wang, Z.; Chang, J.; Fox, P. M.; Bao, Z. Biodegradable and Flexible Arterial-Pulse Sensor for the Wireless Monitoring of Blood Flow. *Nat. Biomed. Eng.* **2019**, *3* (1), 47−57.
(65) Hannah, S.; Brige, P.; Ravichandran, A.; Ramuz, M. Conformable Stretchable Sensor to Record Bladder Wall Stretch. *ACS Omega* **2019**, *4* (1), 1907−1915.
(66) Phan, H. P.; Nguyen, T. K.; Dinh, T.; Cheng, H. H.; Mu, F.; Iacopi, A.; Hold, L.; Dao, D. V.; Suga, T.; Senesky, D. G.; Nguyen, N. T. Strain Effect in Highly-Doped n-Type 3C-SiC-on-Glass Substrate for Mechanical Sensors and Mobility Enhancement. *Phys. Status Solidi* **2018**, *215* (24), 1800288.
(67) Tong, B.; Nguyen, T. H.; Nguyen, H. Q.; Nguyen, T. K.; Nguyen, T.; Dinh, T.; Vo Ke Thanh, N.; Huu Ly, T.; Chi Cuong, N.; Ba Cuong, H.; Xuan Thang, T.; Thanh Dau, V.; Viet Dao, D. Highly Sensitive and Robust 3C-SiC/Si Pressure Sensor with Stress Amplification Structure. *Mater. Des.* **2022**, *224*, 111297.
(68) Souri, H.; Banerjee, H.; Jusufi, A.; Radacsi, N.; Stokes, A. A.; Park, I.; Sitti, M.; Amjadi, M. Wearable and Stretchable Strain Sensors: Materials, Sensing Mechanisms, and Applications. *Adv. Intell. Syst.* **2020**, *2* (8), 2000039.
(69) Amjadi, M.; Kyung, K.-U.; Park, I.; Sitti, M. Stretchable, Skin-Mountable, and Wearable Strain Sensors and their Potential Applications: A Review. *Adv. Funct. Mater.* **2016**, *26* (11), 1678−1698.
(70) Duan, L.; D'hooge, D. R.; Cardon, L. Recent Progress on Flexible and Stretchable Piezoresistive Strain Sensors: From Design to Application. *Prog. Mater. Sci.* **2020**, *114*, 100617.
(71) Gu, G. Y.; Zhu, L. M.; Su, C. Y.; Ding, H.; Fatikow, S. Modeling and Control of Piezo-Actuated Nanopositioning Stages: A Survey. *IEEE Trans. Autom. Sci. Eng.* **2016**, *13* (1), 313−332.
(72) Hassani, V.; Tjahjowidodo, T.; Do, T. N. A Survey on Hysteresis Modeling, Identification and Control. *Mech. Syst. Signal Process.* **2014**, *49* (1−2), 209−233.
(73) Wang, L.; Zhu, R.; Li, G. Temperature and Strain Compensation for Flexible Sensors Based on Thermosensation. *ACS Appl. Mater. Interfaces* **2020**, *12* (1), 1953−1961.
(74) Zhao, S.; Zhu, R. Flexible Bimodal Sensor for Simultaneous and Independent Perceiving of Pressure and Temperature Stimuli. *Adv. Mater. Technol.* **2017**, *2* (11), 1700183.
(75) Phan, H. P.; Dao, D. V.; Nakamura, K.; Dimitrijev, S.; Nguyen, N. T. The Piezoresistive Effect of SiC for MEMS Sensors at High Temperatures: A Review. *J. Microelectromech. Syst.* **2015**, *24* (6), 1663−1677.
(76) Phan, H. P.; Viet Dao, D.; Tanner, P.; Wang, L.; Nguyen, N. T.; Zhu, Y.; Dimitrijev, S. Fundamental Piezoresistive Coefficients of P-Type Single Crystalline 3C-SiC. *Appl. Phys. Lett.* **2014**, *104* (11), 111905.
(77) Moqadam, S. M.; Grewal, P. K.; Haeri, Z.; Ingledew, P. A.; Kohli, K.; Golnaraghi, F. Cancer Detection Based on Electrical Impedance Spectroscopy: A Clinical Study. *J. Electr. Bioimpedance* **2018**, *9* (1), 17.
(78) Hu, S.; Gao, G.; Hong, Z.; Liu, C.; Liu, K.; Yao, J. An Electrode Array Sensor for Tongue Cancer Detection with Bioelectrical Impedance Spectroscopic Tomography. *IEEE Sens. J.* **2022**, *22* (15), 15146−15153.
(79) Chakraborty, A.; Dutta, P.; Wakankar, A.; RoyChaudhuri, C. Recent Field Effect Transistors and Electrical Impedance Spectroscopy Based Biosensing Strategies for Cancer Biomarker Screening: A Mini Review. *Biosens. Bioelectron. X* **2022**, *12*, 100253.
(80) Cheng, Z.; Dall'Alba, D.; Schwaner, K. L.; Fiorini, P.; Savarimuthu, T. R. Robot Assisted Electrical Impedance Scanning for Tissue Bioimpedance Spectroscopy Measurement. *Measurement* **2022**, *195*, 111112.
(81) Pathiraja, A. A.; Weerakkody, R. A.; von Roon, A. C.; Ziprin, P.; Bayford, R. The Clinical Application of Electrical Impedance Technology in the Detection of Malignant Neoplasms: A Systematic Review. *J. Transl. Med.* **2020**, *18* (1), 227.
(82) Tan, H.; Rossa, C. Electrical Impedance Tomography for Robot-Aided Internal Radiation Therapy. *Front. Bioeng. Biotechnol.* **2021**, *9*, 698038.
(83) Chatelin, S.; Bernal, M.; Deffieux, T.; Papadacci, C.; Flaud, P.; Nahas, A.; Boccara, C.; Gennisson, J. L.; Tanter, M.; Pernot, M. Anisotropic Polyvinyl Alcohol Hydrogel Phantom for Shear Wave Elastography in Fibrous Biological Soft Tissue: A Multimodality Characterization. *Phys. Med. Biol.* **2014**, *59* (22), 6923.
(84) Ahuja, A. K.; Behrend, M. R.; Whalen, J. J.; Humayun, M. S.; Weiland, J. D. The Dependence of Spectral Impedance on Disc Microelectrode Radius. *IEEE Trans. Biomed. Eng.* **2008**, *55* (4), 1457−1460.
(85) Fan, J. A.; Yeo, W. H.; Su, Y.; Hattori, Y.; Lee, W.; Jung, S. Y.; Zhang, Y.; Liu, Z.; Cheng, H.; Falgout, L.; Bajema, M.; Coleman, T.; Gregoire, D.; Larsen, R. J.; Huang, Y.; Rogers, J. A. Fractal Design Concepts for Stretchable Electronics. *Nat. Commun.* **2014**, *5* (1), 1−8.
(86) Shan, D.; Sun, D.; Tang, M.; Yang, R.; Kang, G.; Tao, T.; Cao, Y. Structures, Electronic Properties and Carrier Transport Mechanisms of Si Nano-Crystalline Embedded in the Amorphous SiC Films with Various Si/C Ratios. *Nanomater* **2021**, *11* (10), 2678.
(87) Bernardin, E. K.; Frewin, C. L.; Everly, R.; Ul Hassan, J.; Saddow, S. E. Demonstration of a Robust All-Silicon-Carbide Intracortical Neural Interface. *Micromachines* **2018**, *9* (8), 412.
(88) Ivanov, P. A.; Mynbaeva, M. G.; Saddow, S. E. Effective Carrier Density in Porous Silicon Carbide. *Semicond. Sci. Technol.* **2004**, *19* (3), 319.
(89) Saddow, S. E.; Melnychuk, G.; Mynbaeva, M.; Nikitina, I.; Vetter, W. M.; Jin, L.; Dudley, M.; Shamsuzzoha, M.; Dmitriev, V.; Wood, C. E. C. Structural Characterization of SiC Epitaxial Layers Grown on Porous SiC Substrates. *Mater. Res. Soc. Symp.* **2000**, *640* (1), 27.
(90) Rosenbloom, A. J.; Sipe, D. M.; Shishkin, Y.; Ke, Y.; Devaty, R. P.; Choyke, W. J. Nanoporous SiC: A Candidate Semi-Permeable Material for Biomedical Applications. *Biomed. Microdevices* **2004**, *6*, 261−267.
(91) Rosenbloom, A. J.; Shishkin, Y.; Sipe, D. M.; Ke, Y.; Devaty, R. P.; Choyke, W. J. Porous Silicon Carbide as a Membrane for Implantable Biosensors. *Mater. Sci. Forum* **2004**, *457−460*, 1463−1466.
(92) Rosenbloom, A. J.; Nie, S.; Ke, Y.; Devaty, R. P.; Choyke, W. J. Columnar Morphology of Porous Silicon Carbide as a Protein-Permeable Membrane for Biosensors and Other Applications. *Mater. Sci. Forum* **2006**, *527−529*, 751−754.
(93) Piret, G.; Hébert, C.; Mazellier, J. P.; Rousseau, L.; Scorsone, E.; Cottance, M.; Lissorgues, G.; Heuschkel, M. O.; Picaud, S.;

https://doi.org/10.1021/acsnano.4c15294
ACS Nano 2025, 19, 1642−1659

Bergonzo, P.; Yvert, B. 3D-Nanostructured Boron-Doped Diamond for Microelectrode Array Neural Interfacing. *Biomaterials* **2015**, *53*, 173−183.
(94) He, Y.; Tsutsui, M.; Zhou, Y.; Miao, X. S. Solid-State Nanopore Systems: From Materials to Applications. *NPG Asia Mater.* **2021**, *13* (1), 1−26.
(95) Nair, V.; Yi, J.; Isheim, D.; Rotenberg, M.; Meng, L.; Shi, F.; Chen, X.; Gao, X.; Prominski, A.; Jiang, Y.; Yue, J.; Gallagher, C. T.; Seidman, D. N.; Tian, B. Laser Writing of Nitrogen-Doped Silicon Carbide for Biological Modulation. *Sci. Adv.* **2020**, *6* (34), No. eaaz2743.
(96) Hedayati, R.; Ziaei-Rad, S.; Eyvazian, A.; Hamouda, A. M. Bird Strike Analysis on a Typical Helicopter Windshield with Different Lay-Ups. *J. Mech. Sci. Technol.* **2014**, *28* (4), 1381−1392.

https://doi.org/10.1021/acsnano.4c15294
ACS Nano 2025, 19, 1642−1659